Radical-based degradation of Sulfamethoxazole via UVA/PMS-assisted photocatalysis, driven by magnetically separable Fe_3O_4@CeO_2@BiOI nanospheres

Mona Kohantorabi[1], Gholamreza Moussavi[1*], Paula Oulego[2], Stefanos Giannakis[3]

1) Department of Environmental Health Engineering, Faculty of Medical Sciences, Tarbiat Modares University, Tehran, Iran

2) Department of Chemical and Environmental Engineering, University of Oviedo, C/ Julián Clavería s/n., Oviedo, E-33071, Spain

3) Universidad Politécnica de Madrid, E.T.S. Ingenieros de Caminos, Canales y Puertos, Departamento de Ingeniería Civil: Hidráulica, Energía y Medio Ambiente, Unidad docente Ingeniería Sanitaria, c/ Profesor Aranguren, s/n, ES-28040 Madrid, Spain

**Corresponding author: Prof. Dr. Gholamreza Moussavi, Email: moussavi@modares.ac.ir*

Published in "Separation and Purification Technology", Elsevier:

https://www.sciencedirect.com/science/article/abs/pii/S1383586621003774

Permanent Address (DOI):

https://doi.org/10.1016/j.seppur.2021.118665

Abstract

In this work, novel magnetic Fe_3O_4@CeO_2@BiOI nanospheres were synthesized for the heterogeneous photocatalytic activation of peroxymonosulfate (PMS) towards sulfamethoxazole (SMX) degradation. The phase purity, morphology, and surface properties of the nanocomposite were fully characterized and confirmed the formation of a heterojunction between the magnetic Fe_3O_4@CeO_2 and BiOI. Low catalyst (0.1 g/L) and PMS addition (0.2 mM) under UVA-LED light irradiation led to high catalytic activity in SMX degradation (97%, k_{app} = 0.221 min^{-1}) within 15 min. The highest quantum yield (QY) value (5.02×10^{-4} molecules $photon^{-1}$) was measured for the ternary Fe_3O_4@CeO_2@BiOI nanocomposite, which is 3.54, 3.76, and 4.04 times higher than Fe_3O_4@CeO_2, BiOI, and CeO_2 coupled with PMS/UVA, respectively. Furthermore, different experimental conditions, including initial solution pH, catalyst:PMS ratio, water matrix ions on the Fe_3O_4@CeO_2@BiOI/PMS/UVA system, were investigated under the optimum reaction conditions. As deduced from the LC/MS analysis, the possible SMX degradation pathways were proposed. Based on radicals scavenging experiments, $SO_4^{\bullet-}$, $HO^{\bullet}$, and $O_2^{\bullet-}$ are mainly involved in SMX degradation. Finally, recycling and leaching experiments confirmed a stable material with coherent catalytic performance for the activation of PMS by Fe_3O_4@CeO_2@BiOI catalyst under UVA, with excellent magnetic recovery capabilities. As such, this material has high potential for degradation of organic contaminants and in extension for water treatment processes.

Keywords: Magnetic photocatalyst; Peroxymonosulfate activation; Antibiotic degradation; Advanced oxidation processes (AOPs); Nanoparticles.

Highlights

- Fe_3O_4@CeO_2@BiOI nanosphere was synthesized by using hydrothermal method.
- The addition of PMS produced the synergetic effect in Fe_3O_4@CeO_2@BiOI photocatalytic system under UVA.
- 97% of sulfamethoxazole (SMX) could be removed from the reaction within 15 min with rate constant value of 0.221 min^{-1}.
- $HO^{\bullet}$, $SO_4^{\bullet-}$, and $O_2^{\bullet-}$ were dominant reactive species which involved in SMX degradation pathway.

Graphical Abstract

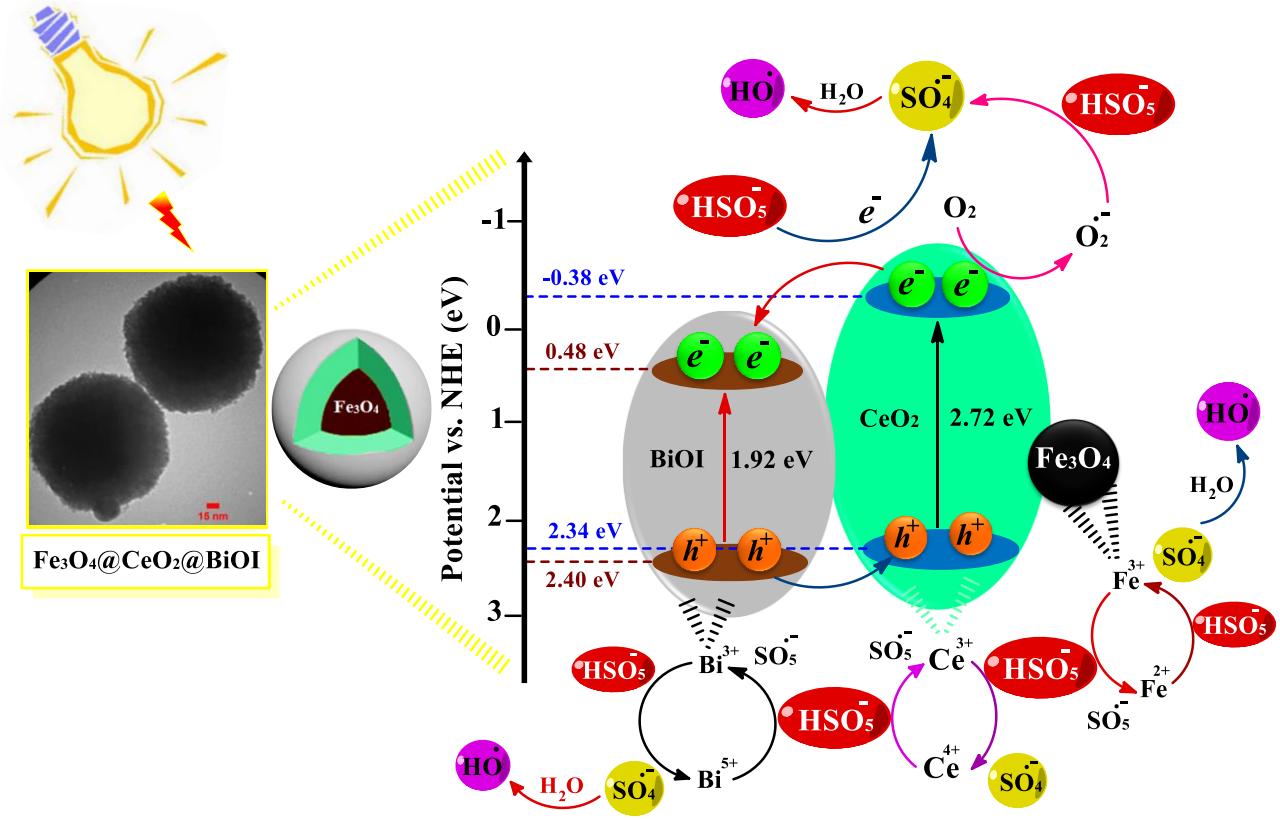

1. Introduction

During the last decades, the excess administering and use of antibiotics has caused increasing concern on the public health and natural water ecosystems' balance (Huang et al. 2019). Among these antibiotics, sulfamethoxazole (SMX) is a sulfonamide antibiotic that has been widely used for the treatment of bronchitis and other infections (Yazdanbakhsh et al. 2020). SMX has been detected in various environmental matrices, such as surface water and groundwater, at different concentrations, i.e., from ng/L to mg/L (Chen et al. 2019). Antibiotics are only partially absorbed by human bodies and animals and are excreted to water and environment through urine and feces (Dong et al. 2018). Hence, effective methods and high-performance processes are required for the removal and degradation of SMX from the effluents, due to its low biodegradability and long-term persistence in the environment (Oh et al. 2017).

Among the different technologies that have been recently employed for the removal of pollutants from water, such as adsorption, biodegradation and separation, advanced oxidation processes (AOPs) have received attention as an effective and promising technology (Liu et al. 2020). In recent years, AOPs based on peroxymonosulfate (HSO_5^-, PMS) have been developed as an effective oxidation method for the removal of contaminants from aqueous matrices (Giannakis et al., 2021a). PMS is considered as a great oxidant due to its high stability, easy activation, and facility of operation at a wide matrix pH range (Ghanbari and Moradi, 2017). Due to the asymmetric structure of PMS, hydroxyl ($HO^{\bullet}$) and sulfate ($SO_4^{\bullet -}$) radicals, with high standard redox potential (1.8–2.7 V, and 2.5–3.1 V *vs*. NHE, respectively) can be generated after its activation (Rodriguez-Chueca et al. 2019). Over the last years, the heterogeneous activation of PMS by transition metal (Me) based catalysts has been developed (Li et al. 2020; Guo et al. 2020a) and the most important advances have been recently reviewed (Kohantorabi et al. 2021a). Due to the presence of $Me^{n+}/Me^{(n+1)+}$ redox cycles of metal ions in catalyst structure, metal oxides have a high capacity in effective PMS activation (eqns. 1, and 2) (Xu et al. 2020), while multi-metallic oxides take advantage of synergic redox reactions among metals (Giannakis et al., 2021b).

$$HSO_5^- + Me^{n+} \longrightarrow SO_4^{\bullet -} + HO^- + Me^{(n+1)+} \quad (1)$$

$$HSO_5^- + Me^{n+} \longrightarrow SO_4^{2-} + HO^{\bullet} + Me^{(n+1)+} \quad (2)$$

Besides, UV irradiation is an effective way to activate PMS, which is used frequently in wastewater treatment (Qi et al. 2019). Under irradiation, PMS can be activated and produce $SO_4^{\bullet -}$ and $HO^{\bullet}$ radicals (eq. 3). In parallel, the advent of LED lamps allows a cheap and effective control over the desired light emission characteristics, which facilitate its application.

$$HSO_5^- + h\nu \longrightarrow HO^{\bullet} + SO_4^{\bullet -} \quad (3)$$

Photocatalytic oxidation is an interesting approach in AOPs, due to the formation of reactive oxygen species (ROS) effective for the degradation of a wide range of contaminants (Mirzaei et al. 2018; Zarezadeh et al. 2019; Vosoughi et al. 2020). Recently, photocatalysts were used as effective catalysts for the activation of PMS even under visible light irradiation (Hu et al. 2019; Zhang et al. 2021). Moreover, apart from PMS direct light activation, photo-produced reactive intermediates (PPRI) such as electron/hole (e^-/h^+) pairs from the photocatalyst can also activate PMS (Shao et al. 2017).

Furthermore, in the search for effective photo-catalysts, the efficiency of a wide range of Bi-based semiconductors such as $BiVO_4$ (Wetchakun et al. 2012), Bi_2MoO_6 (Vaseli-Kermani et al. 2020), Bi_2WO_6 (Yuan et al. 2019), $BiPO_4$ (Gao et al. 2019), and BiOX (X = Cl, Br, and I) (Bardos et al. 2019) has been tested. Among them, BiOI has been highlighted as a promising photocatalyst in environmental applications, due to its remarkable activity, non-toxic nature, low manufacturing cost, and narrow band gap energy (2.19 eV) (Hu et al. 2019; Mehraj et al. 2016). However, due to the fast recombination of the photogenerated e^-/h^+ pairs, the photocatalytic activity of BiOI alone is poor. Hence, modification of BiOI with other semiconductors has been considered as an effective method to improve its photo-activity (Moussavi and Habibi-Yangjeh, 2016). Among the various semiconductors available, CeO_2, a rare earth oxide, has been tested in industrial applications such as fuel cells, catalysis, photocatalysis and solar cell-compatible materials (Jiang et al. 2019; Raso et al. 2014). Due to its high activity, non-toxicity, high stability, and environmentally friendly properties, it has been used in photocatalytic processes (Wen et al. 2017). Nevertheless, the poor visible light absorption capacity, and their low capability to separate e^-/h^+ pairs are the main shortcomings of single CeO_2 (Wen et al. 2017). To overcome these problems of single semiconductors, fabrication of heterojunction can significantly enhance their photocatalytic activity, and separation of photo-generated charge carries (Wang et al. 2020a).

Besides the high activity, suitable band gap and good charge separation, another important challenge in photocatalytic oxidation is the complete and easy separation of the photocatalyst from the reaction media (Khavar et al. 2019). For this purpose, magnetic nanocomposites have been developed in environmental applications, due to their superparamagnetic properties, which allows them to be recovered from the reaction solution by using an external magnetic field (Khavar et al. 2019; Kohantorabi and Gholami 2018a; Ghanbari et al. 2019). Fe_3O_4 is an ideal material for this purpose, with unique features including low cost, high stability, easy preparation, high magnetism, and eco-friendly character (Boruah et al. 2017). Considering the above reasoning, fabrication of magnetic photocatalysts with high activity in PMS activation for the destruction of chemical contaminants is expected to be very effective against antibiotics, while literature has very few works of photocatalysts bridging all these features.

In the present study, a magnetic, multi-layered nanosphere including Fe_3O_4, CeO_2 and BiOI was synthesized by a hydrothermal method, which showed high activity in PMS activation, for antibiotics degradation under UVA-LED light irradiation. The main objectives of this study are: i) to study the role of redox cycles of the metal oxides existing in Fe_3O_4@CeO_2@BiOI in the activation of PMS and formation of reactive species, ii) to investigate the photocatalytic activity of the Fe_3O_4@CeO_2@BiOI/PMS process in the removal of SMX under UVA irradiation, and iii) the evaluation of the stability and recyclability of the as-made nano-catalyst in photocatalytic activation of PMS. In addition, the effect of different reaction conditions (catalyst loading, oxidant concentration), and matrix composition were investigated in SMX degradation reaction. Finally, to provide insight on the mechanistic aspects of sulfonamide antibiotics degradation, the elimination pathway of SMX by the nanocomposite was studied in detail.

2. Materials and Methods

2.1. Chemicals and reagents

Iron chloride hexahydrate ($FeCl_3$. $6H_2O$), sodium acetate (CH_3COONa), cerium nitrate hexahydrate (Ce $(NO_3)_3$. 6 H_2O), ethylene glycol (EG), ethanol (EtOH), ammonium solution (NH_4OH), peroxymonosulfate (PMS, Oxone, $2KHSO_5.KHSO_4.K_2SO_4$), and all scavengers including *tert*-butyl alcohol (TBA), sodium oxalate ($Na_2C_2O_4$, OX), and *p*-benzoquinone (BQ) were purchased from Merck Company. Bismuth nitrate tetrahydrate (Bi $(NO_3)_2$. $4H_2O$), sodium azide (NaN_3, SA), and potassium iodide (KI) were supplied from Sigma Aldrich. Also, all sodium salts including sodium chloride (NaCl), sodium bicarbonate ($NaHCO_3$), sodium sulfate (Na_2SO_4), sodium phosphate (Na_3PO_4), and sodium nitrate ($NaNO_3$) were purchased from Merck. The pure Sulfamethoxazole (SMX) powder was obtained directly from a local supplier (Aria Co. Iran). The stock solution of SMX was obtained by dissolving 0.56 g of SMX in 1.0 L of distilled (DI) water, and stored at 4.0±1.0 °C.

2.2. Analytical chemical and material science techniques

2.2.1. Catalysts' characterization

The phase purity and crystalline structure of as-synthesized samples were evaluated by using X-ray diffraction (XRD) analysis on Philips X'Pert-MPD X-ray diffractometer with a Cu Kα radiation (λ = 1.54060 A°) in the 2Θ range of 10-80°. The surface functional groups of the as-made catalysts were acquired by the Fourier transform infrared spectra (FT-IR, AB BOMER MB Spectrophotometer) in the wavelength range from 400 to 4000 cm^{-1}. To investigate the morphology of samples and their elemental analysis, field emission scanning electron microscopy (FE-SEM, Mira3 Tascan), transmission electron microscopy (TEM, Philips-CM30 instrument), and energy dispersive X-ray spectroscopy (EDX) were applied. For the investigation of the surface composition of the catalyst, and binding energies of elements, X-ray photoelectron spectroscopy (XPS) was carried out with a SPECS Phoibos 100 MCD5 hemispherical electron analyzer operating at a constant pass energy. K_α Mg (1253.6 eV) was the X-ray source employed together with a flood electron gun to compensate charge effects on the catalysts. Survey and high-

resolution spectra were performed with an energy pass of 90 eV and step energy of 1.0 eV, and with an energy pass of 30 eV and step energy of 0.1 eV, respectively.

The optical properties of samples were evaluated by using UV-Vis diffused reflectance spectroscopy (DRS, Shimadzu 2550-8030 spectrophotometer) in the wavelength range from 200 to 800 nm. Moreover, the photoluminescence (PL) spectra of samples were recorded *via* FL3-TCSPC fluorescence spectrophotometer at ambient temperature. Electrochemical impedance spectroscopy (EIS) measurement was provided by using Na_2SO_4 solution (0.3 M) with frequency ranging between 0.1-10^6 Hz. The magnetic properties of samples were measured by using a vibrating sample magnetometer (VSM, PPMS). The specific surface area, and pore size distribution of samples were determined by using Nitrogen adsorption-desorption analysis at 77 K (Micromeritics/Gemini-2372 analyzer).

2.2.2. Sulfamethoxazole degradation process characterization

The concentration of SMX during the reaction was evaluated by high pressure liquid chromatography (HPLC, Eclipse plus C18 column; 3.5 µm, Agilent Co) equipped with a UV detector at 270 nm. The mobile phase was a mixture of acetonitrile and water with a volumetric ratio of 40:60 and injected with a flow rate of 0.8 mL min^{-1}. To study the mechanism pathway, and intermediates generation during the reaction under optimal conditions, liquid-chromatography-mass spectroscopy (LC-MS, 2010 A/Shimadzu) coupled with an Eclipse Atlantis T3, C18 column (2.1×100 mm, 3.0 µ particle size) was used at room temperature. The mobile phase of this analysis consisted of acetonitrile (containing 0.1% formic acid), and water (containing 0.1% formic acid), which was injected at a flow rate of 0.2 mL min^{-1}, and an injection sample volume of 10.0 µL. Also, the following conditions were operated for the Mass spectrophotometer; gas nebulizer: nitrogen (N_2), capillary volt: 4.0 kV, Cone volt: 30 V, flow gas: 3.3 L min^{-1}, and source, and desolation temperatures are 120 °C, and 350 °C, respectively. The spectrophotometer scanning was collected for *m/z* in the ranging of 50-500. The pH_{ZPC} value of as-made nanocomposite was determined based on changes of the pH values of KNO_3 solution as electrolyte (Ghanbari et al. 2019). The total organic carbon (TOC) of samples was measured using a Shimadzu TOC Analyzer (TOC-L CSH/CSN). Finally, the concentration

of PMS during the reaction was evaluated by using iodo-metric method (Vogel 1989) and solution pH was measured by Jenway pH-meter (Jenway Co. UK).

2.3. Synthesis of Fe_3O_4 nanoparticles, Fe_3O_4@CeO_2 and Fe_3O_4@CeO_2@BiOI nanospheres

2.3.1. Magnetite (Fe_3O_4) nanoparticle synthesis

Magnetic Fe_3O_4 nanoparticles (NPs) were synthesized by a common hydrothermal method (Kohantorabi and Gholami, 2018a). Briefly, 4.4 mmol (1.20 g) of $FeCl_3{\cdot}6H_2O$ was dissolved in 75 mL of ethylene glycol (EG) for 15 min under stirring. Then, 44.0 mmol (3.60 g) of sodium acetate was added into the above mixture under stirring. The suspension was stirred for 30 min at ambient temperature. Following, the mixture was transferred into a Teflon-lined steel autoclave and heated at 200 °C for 16 h. After cooling to room temperature, the black products were separated from the reaction media by using an external magnet, washed three times with a water/ethanol mixture, and then dried at 70 °C overnight.

2.3.2. Fe_3O_4@CeO_2 synthesis

The CeO_2 was synthesized on magnetic NPs by using a hydrothermal method. According to this method, a certain amount of as-made Fe_3O_4 was dispersed into the 30 mL of EG under sonication for 20 min as solution A. In another vial, 2.3 mmol (1.0 g) of Ce $(NO_3)_3$. $6H_2O$ was dissolved in 5.0 mL of DI water. After dissolving, 1.0 mL of acetic acid, and 30 mL of EG were added into the suspension under ultrasonic treatment at room temperature. After mixing for 30 min, the obtained solution was added into the solution A under continuous stirring. Afterwards, the mixture was immediately transferred into the Teflon-lined autoclave, and heated at 180 °C for 200 min, then cooled to room temperature. The resultant product (Fe_3O_4@CeO_2) was washed with ethanol and water, and then dried at 70 °C for 8 h. The pure CeO_2 NPs were synthesized by using the same method without the addition of Fe_3O_4 (Kohantorabi and Gholami 2018b).

2.3.3. Fe_3O_4@CeO_2@BiOI nanospheres' synthesis

The BiOI was prepared on the surface of magnetic Fe_3O_4@CeO_2 catalyst by using hydrothermal method. In this procedure, 0.2 g of the synthesized Fe_3O_4@CeO_2 catalyst was dispersed in to 25.0 mL of DI water under sonication,

and named solution A. Then, 20 mL of Bi $(NO_3)_2$. $4H_2O$ (0.3 M) was added dropwise into the suspension under continuous stirring. After 10 min, 25 mL of KI solution (0.2 M) was added dropwise and the mixture was stirred for 30 min. Afterwards, the resultant suspension was transferred to the Teflon-lined autoclave and heated at 140 °C for 12 h. After completing the reaction, the autoclave was cooled to room temperature and the obtained products were separated from the solution by using a magnet, washed with a water/ethanol solution, and finally dried at 70 °C overnight. The pure BiOI catalyst was synthesized by the same procedure, without addition of Fe_3O_4@CeO_2 catalyst. Scheme 1 illustrates the synthesis steps involved in the preparation of Fe_3O_4@CeO_2@BiOI nanospheres.

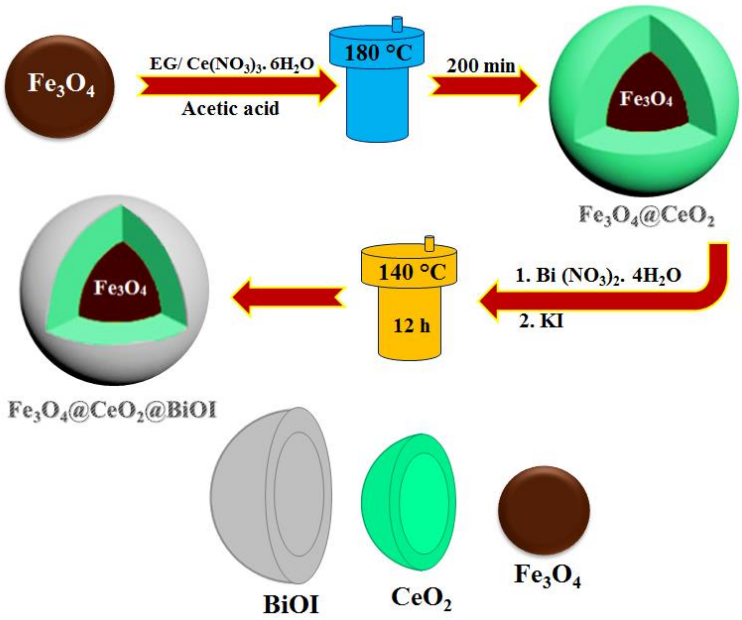

Scheme 1. Schematic of the synthesis steps of Fe_3O_4@CeO_2@BiOI nanosphere.

2.4. Photo-catalytic SMX degradation testing procedure

To investigate the catalytic activity of the as-made samples including Fe_3O_4, CeO_2, BiOI, Fe_3O_4@CeO_2, CeO_2@BiOI, and Fe_3O_4@CeO_2@BiOI, the degradation of SMX in the presence of PMS under UVA was selected. The working solution of SMX was obtained from the stock solution. The reaction was carried out in a photo-reactor with total volume of 50 mL, and an inner diameter around 10 cm. A quartz sheet was introduced under the top of reactor that LED setup was placed on it. The distance between reaction solution, and LED setup which involved 19 light-emitting diodes (Seoul Semiconductor, South Korea) with wavelength at 365 nm, was 1.0 cm. In each catalytic

reaction, a certain amount of catalyst was dispersed in to 20 mL of the SMX solution (0.05 mM) and transferred into the reactor. Then, 200 µL of PMS (20 mM) was added into the reaction solution, and magnetically stirred under LED irradiation. After pre-determined interval times, 1.0 mL of reaction solution was taken, and filtered by using 0.22-µL PTFE membranes. The removal of SMX was evaluated by HPLC analysis. The control experiments including light alone, PMS alone, and catalyst in the dark were done under the same reaction conditions. Moreover, the initial pH solution was adjusted by NaOH, and H_2SO_4 (0.05 mM) solutions. All experiments were performed in duplicate, and the obtained results were reported by the average ± standard deviation. To further study the role of ROS, and photo-generated species during the reaction, scavenging tests in the presence of TBA, BQ, EtOH, OX, and SA for the sequestering of $HO^{\bullet}$, $O_2^{\bullet-}$, $SO_4^{\bullet-}$ and $HO^{\bullet}$ (jointly), h^+, and singlet oxygen ($^1O_2$) respectively, were carried out under the optimum conditions.

2.5. Cycling experiments

The stability and recyclability of as-prepared catalyst was tested in consecutive catalytic cycles under the "optimal" conditions (best catalyst/oxidant ratio) of SMX oxidation. After each catalytic reaction, the nanocomposite was separated from the reaction media by an external magnetic field, washed three times with water/ethanol to remove all substrates from the surface of catalyst, and then dried at 70 °C overnight. Afterwards, the catalytic performance of the reused catalyst was investigated in the degradation of SMX coupled with PMS/UVA as described before, in Section 2.4.

2.6. Performance indices

The concentration of SMX during the reaction was detected by using HPLC and the removal efficiency (%) was calculated by the following equation (eq. 4):

$$Removal\ efficiency\ (\%) = \frac{SMX_0 - SMX_t}{SMX_0} \times 100 \quad (4)$$

In which, SMX_0, and SMX_t are the concentration of SMX at beginning and time t of reaction, respectively. Also, the mineralization of SMX was investigated by using equation 5 under optimum reaction conditions based on TOC

measurement. In this equation, the TOC_0, and TOC_t are the TOC concentrations of SMX at time zero and t of the reaction, respectively.

$$Mineralization\ (\%) = \frac{TOC_0 - TOC_t}{TOC_0} \times 100 \quad (5)$$

To investigate the reaction rate constant of reaction, the pseudo-first order (PFO) reaction model was applied, and the values were calculated from the eq. 6.

$$\ln\left(\frac{C_t}{C_0}\right) = -k_{app}t \quad (6)$$

In addition, the observe PFO rate (r_{obs}, mg L^{-1} min^{-1}) of SMX degradation was calculated by using the eq. 7.

$$r_{obs} = -k_{app}C_0 \quad (7)$$

C_t, and C_0 are the concentration of SMX at beginning and time t of reaction in mg L^{-1}. The k_{app} and r_{obs} values of SMX degradation were obtained by fitting eqns. 6 and 7, respectively.

The quantum yield (φ, QY) of the photocatalytic system was calculated by using the eq. 8. QY factor can be used for the evaluation of photocatalytic performance (Reza et al. 2020).

$$Quantum\ yield = \frac{Decay\ rate\ (molecule\ per\ second)}{Photon\ flux\ (Photons\ per\ second)} \quad (8)$$

Also, the Figure of Merit (FoM) parameter was calculated for this photocatalytic system (eq. 9), which is a meaningful evaluation for photocatalytic process (Vikrant et al. 2019). This parameter involved all the relevant performance variables, actual comparisons performance of aqueous photocatalytic system can be obtained.

$$\mathrm{FoM} = \frac{\text{Conversion efficiency (\%)}}{\text{Catalyst mass (mg)} \times [\text{concentration}]_0\ \text{(ppm)} \times \text{Irradiation time (min)} \times \text{Applied power (W)}} \quad (9)$$

3. Results and discussion

3.1. Characterization of the synthesized nano-catalysts

To study the functional groups that are present on the synthesized catalysts, FT-IR analysis was performed, and the obtained results are illustrated in Fig. 1A. For the pure CeO_2 NPs, the peak centered at 561 cm^{-1} can be assigned to the Ce−O (Wen et al. 2017). In the FT-IR spectra of Fe_3O_4, the peak around 575 cm^{-1} is attributed to the Fe−O lattice model of Fe_3O_4 (Khavar et al. 2019). Both peaks were observed in FT-IR spectrum of Fe_3O_4@CeO_2@BiOI nanocomposite that confirmed the successful synthesis of the magnetic catalyst (Fig. 1A). It should be noted that the wide range peak around 3400-3500 cm^{-1} in the FT-IR spectra of all samples is related to the hydroxyl band (−HO) of the adsorbed water on the surface of catalyst. The absorption peak displayed at 489 cm^{-1} is related to the stretching vibration mode of the Bi−O. Also, the broad characteristic signal at 1587 cm^{-1} corresponds to the stretching vibration of the −HO group (Zhong et al. 2019). The presence of the peaks in the FT-IR spectrum of Fe_3O_4@CeO_2@BiOI nanocomposite indicated the successful loading of BiOI shell on the Fe_3O_4@CeO_2 catalyst.

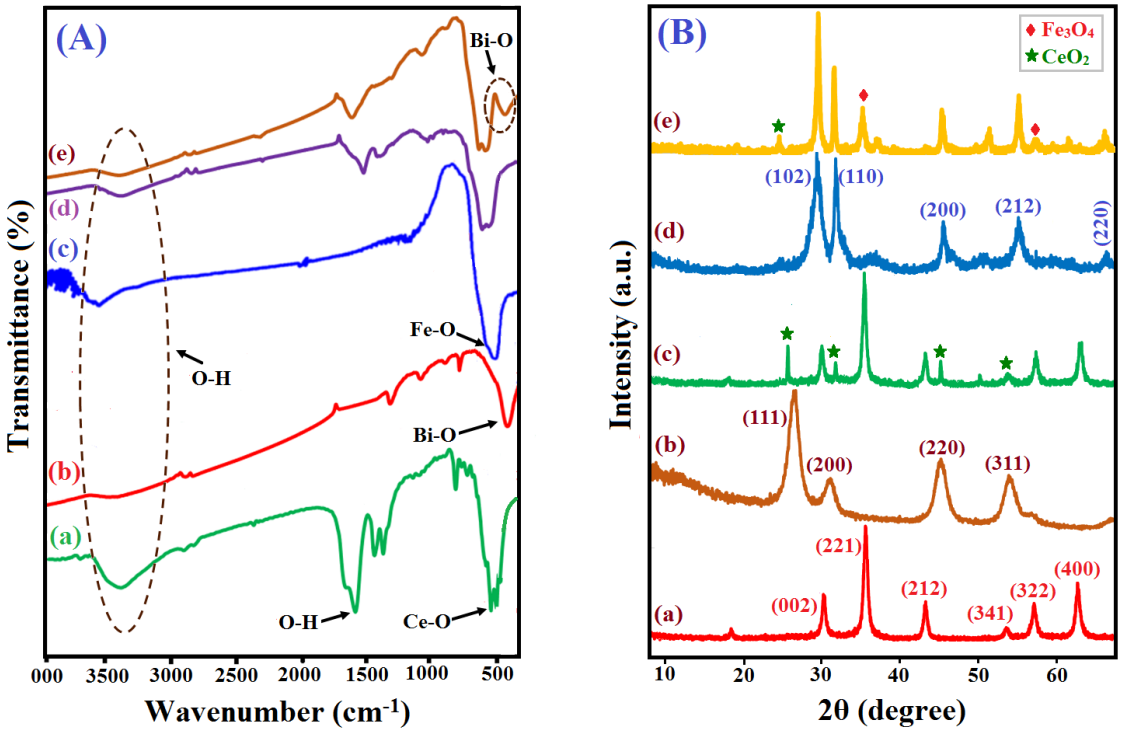

Figure 1. (A) FT-IR spectra of CeO_2 NPs (a), BiOI (b), Fe_3O_4 (c), Fe_3O_4@CeO_2 (d), and Fe_3O_4@CeO_2@BiOI (e). (B) XRD patterns of Fe_3O_4 (a), CeO_2 (b), Fe_3O_4@CeO_2 (c), BiOI (d), and Fe_3O_4@CeO_2@BiOI (e).

The phase purity and crystalline structure of Fe_3O_4, CeO_2, BiOI, Fe_3O_4@CeO_2, and Fe_3O_4@CeO_2@BiOI nanocomposites was investigated using XRD analysis. The XRD patterns of all samples were reported in Fig. 1B. In the pattern of Fe_3O_4 NPs, the diffraction peaks located at 31.97°, 35.47°, 43.46°, 53.53°, 57.04°, and 62.67° are assigned to the (002), (221), (212), (341), (322), and (400) planes, respectively (JCPDS No. 98-001-7260) (Kohantorabi and Gholami, 2018a). The characteristic peaks centered at 28.50°, 33.10°, 45.52°, and 56.34° correspond to the (111), (200), (220), and (311) crystalline structure of CeO_2 NPs (JCPDS No. 00-004-0593) (Wang et al. 2020a). The diffraction peaks related to the (111), (200), and (220) plane of cubic structure of pure CeO_2 NPs were observed in XRD pattern of Fe_3O_4@CeO_2 nanocomposite. The XRD pattern of the pure BiOI nanostructure exhibited five strong diffraction peaks centered at 29.61°, 31.62°, 45.37°, 55.15°, and 67.21° which are related to the (102), (110), (200), (212), and (220) planes of BiOI structure (Jiang et al. 2019). As can be seen from the XRD pattern of the magnetic Fe_3O_4@CeO_2 catalyst, the characteristic peaks related to the Fe_3O_4, and CeO_2 were observed in the spectra, and confirmed the successful formation of the CeO_2 on the surface of the magnetic core (Fig. 1B). Moreover, the crystal phase of BiOI was preserved in as-made Fe_3O_4@CeO_2@BiOI nanocomposite, which confirmed the successful formation of this nanocomposite by the reported method. Also, due to the presence of the BiOI on the surface of Fe_3O_4@CeO_2 nanospheres, the intensity of diffraction peaks related to Fe_3O_4, and CeO_2 was decreased in XRD pattern of Fe_3O_4@CeO_2@BiOI nanocomposite (Fig. 1B).

The microscopic morphologies of our synthesized catalysts are shown in Fig. 2. Fig. 2 a-c shows the TEM images of Fe_3O_4@CeO_2@BiOI nanocomposite that prove its spherical structure. As can be seen from the Fig. 2a, the as-synthesized catalyst is uniform. According to the TEM analysis, CeO_2 and BiOI were successfully coated on the surface of Fe_3O_4 NPs. The FE-SEM image of Fe_3O_4@CeO_2@BiOI nanocomposite exhibited the spherical structure of as-made nanocomposite (Fig. 2d). As presented in Fig. 2e through 2j, iron (Fe), cerium (Ce), oxygen (O), bismuth (Bi), and iodine (I) were distributed in as-prepared catalyst. To study the chemical composition of the nanoparticles, the energy dispersive X-ray (EDX) analysis was applied. The presence of elements including Ce, Fe, Bi, I, and O was confirmed from the EDX spectrum, suggesting the formation of the Fe_3O_4@CeO_2@BiOI nanocomposite (Fig. 2k). Although the amount of CeO_2 on the surface of magnetic core was low, the characteristics peak of Ce in EDX spectra of the as-made nanocomposite confirmed the presence of CeO_2.

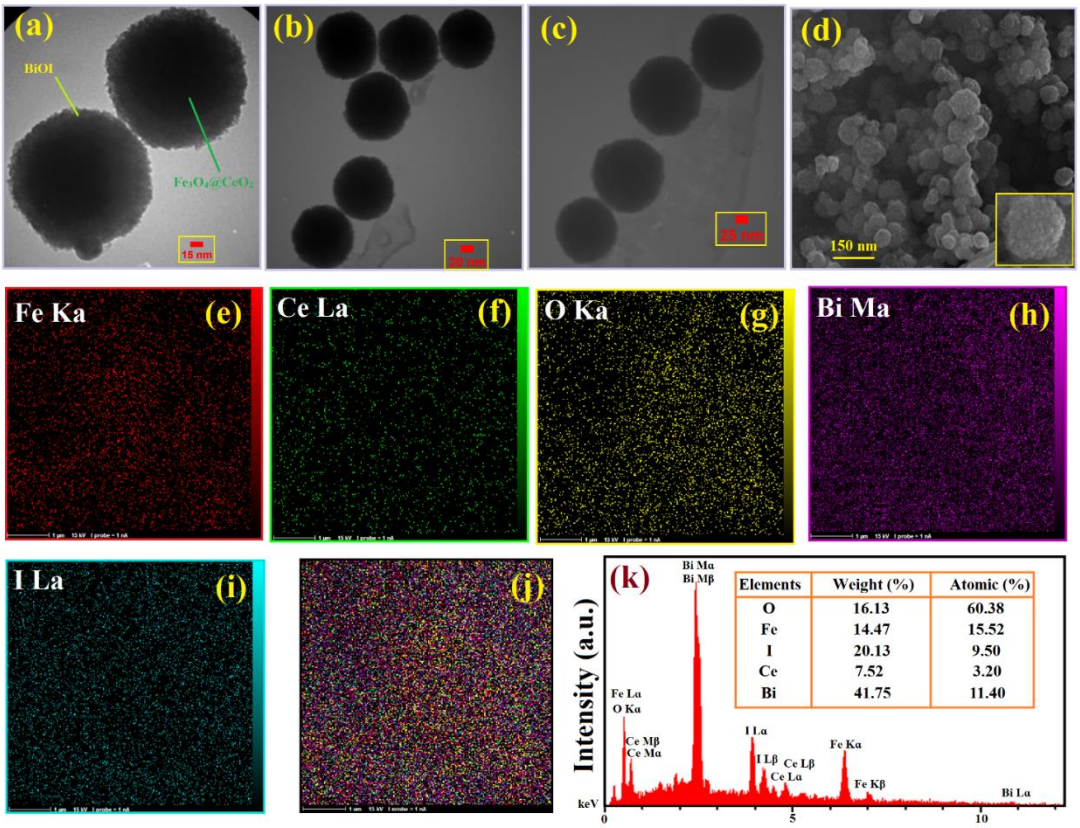

Figure 2. TEM images (a-c), and FE-SEM image (d) of Fe_3O_4@CeO_2@BiOI nanocomposite. Elemental mapping of iron (e), cerium (f), oxygen (g), bismuth (h), iodine (i), and Fe_3O_4@CeO_2@BiOI (j), and EDX analysis of Fe_3O_4@CeO_2@BiOI nanocomposite (k).

The detailed chemical composition of Fe_3O_4@CeO_2@BiOI nanospheres was obtained by XPS analysis (Fig. 3). Fig. 3a shows the XPS survey spectra of the nanospheres, which confirmed the presence of Fe, Ce, Bi, I and O, and indicated the coexistence of all three catalysts in the as-prepared ternary nanocomposite. The high-resolution XPS spectra of Fe2p, Ce3d, O1s, Bi4f, and I3d are shown in Fig. 3b-k. Regarding the Fe2p spectrum (Fig. 3b), the deconvolution of the $Fe2p_{3/2}$, and $Fe2p_{1/2}$ were observed at binding energies 711.2 eV, and 724.8 eV, respectively (Boruah et al. 2017). It is found that there is an energy separation of 13.6 eV between $Fe2p_{1/2}$, and $Fe2p_{3/2}$ peaks that is in good agreement with literature (Khavar et al. 2019). Both these peaks confirmed the presence of both Fe^{2+}, and Fe^{3+} in Fe_3O_4 structure. The high-resolution spectra of Ce3d demonstrated two main peaks at 902.4 eV, and 883.5 eV that are classified as the spin splitting orbits of $3d_{3/2}$, and $3d_{5/2}$ of Ce ion (Wang et al. 2015). Both these peaks confirmed the presence of Ce with oxidation state of 3+. Moreover, these peaks may be deconvoluted to the

small peaks at 886.3 eV, 898.2 eV, 905.6 eV, and 917.0 eV labeled with ♦ in Fig. 3d, which are corresponding to Ce^{4+} (Wang et al. 2015). In the XPS spectrum of Bi4f (Fig. 3h), two binding energies located at 159.5 eV, and 164.8 eV are corresponding to the $Bi4f_{7/2}$, and $Bi4f_{5/2}$ and indicated the presence of Bi^{3+} ions in BiOI nanostructure (Hou et al. 2017). Moreover, the high-resolution I3d XPS spectrum (Fig. 3j) exhibits two peaks at binding energies at 619.4 eV, and 630.9 eV, which correspond to the $I3d_{5/2}$, and $I3d_{3/2}$, respectively (Jiang et al. 2019; Hou et al. 2017). The XPS spectrum of O1s (Fig. 3f) shows two peaks at 530.4 eV, and 528.2 eV that can be assigned to the Bi-O, and Ce-O bonds in BiOI and CeO_2 structures, respectively (Jiang et al. 2019). Moreover, the peaks at 533.3 eV, and 532.2 eV in spectrum of O1s were attributed to the physically adsorbed H_2O and hydroxyl groups, respectively (Jiang et al. 2019). Based on the above results, the planned Fe_3O_4@CeO_2@BiOI ternary catalyst was successfully synthesized by the hydrothermal method reported in this study.

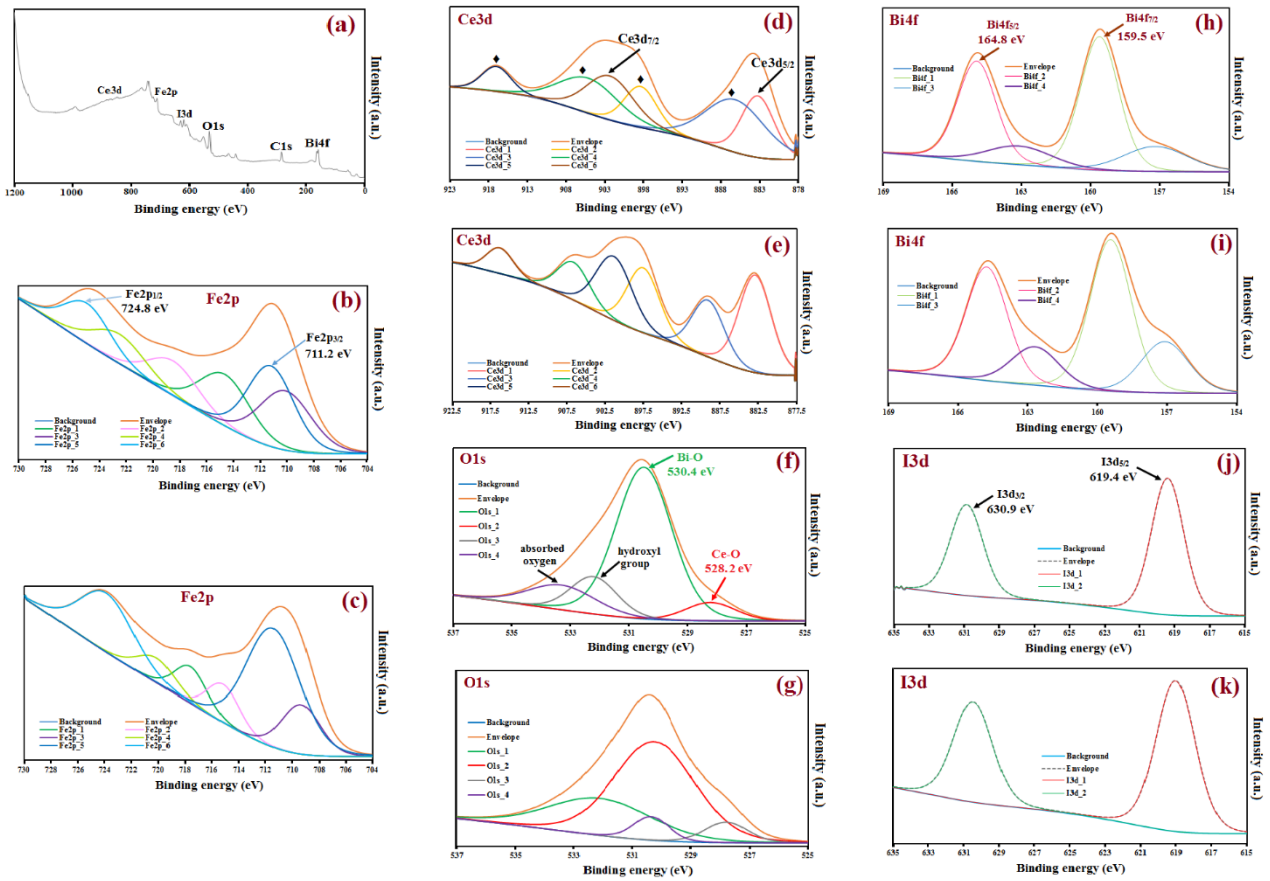

Figure 3. XPS survey spectra of Fe_3O_4@CeO_2@BiOI nanocomposite (a), and the high-resolution spectra of Fe2p (b, c), Ce3d (d, e), O1s (f, g), Bi4f (h, i), and I3d (j, k) fresh and reused catalyst, respectively.

The optical absorption properties and band gap energies (E_g) of the as-synthesized catalysts were determined by UV-Vis DRS analysis. Fig. 4a shows the UV-Vis DRS spectra of BiOI, CeO_2, Fe_3O_4@CeO_2, and Fe_3O_4@CeO_2@BiOI nanocomposites. It is obvious that after doping BiOI on the surface of the magnetic catalyst, the absorption edge of Fe_3O_4@CeO_2 nanocomposite was red-shifted, which is related to the enhanced light absorption ability of the new catalyst. The high photocatalytic performance of Fe_3O_4@CeO_2@BiOI nanocomposite can be related to the wide light absorption, which can enhance the generation of more e^-/h^+ pairs during the reaction under light irradiation. The optical E_g of the as-made samples were calculated by equation 10, where *a*, *h*, *v*, and A correspond to the absorption coefficient, Plank's constant, light frequency and constant, respectively (Salari and Kohantorabi, 2020). In this equation, the value of n is 1/2, and 2 for the direct, and indirect band gap semiconductors, respectively (Huang et al. 2017).

$$\alpha h\nu = A\,(h\nu - E_g)^{1/n} \qquad (10)$$

Based on this equation, the E_g values of CeO_2, BiOI, Fe_3O_4@CeO_2, and Fe_3O_4@CeO_2@BiOI nanocomposite were calculated to be 2.72 eV, 1.92 eV, 1.12 eV, and 1.46 eV, respectively, derived from the plot of $(ahv)^2$ against E_g (Fig. 4b). As it can be seen from the obtained results, the presence of the BiOI shell on the surface of the binary nanocomposite can decrease the band gap energy of the photocatalyst, which in turn can cause the high photocatalytic performance under UVA light.

To further investigate the photocatalytic properties, owing to the recombination of photo-generated carrier, the photoluminescence (PL) spectra were studied. Fig. 4c displays the PL spectra of the Fe_3O_4, BiOI, Fe_3O_4@CeO_2, and Fe_3O_4@CeO_2@BiOI nanocomposite, using an excitation wavelength at 365 nm. In the PL spectra, the lower PL intensity indicates the high separation efficiency of photo-generated e^-/h^+ pairs (Jiang et al. 2019). Based on the results, in comparison with pristine BiOI, the as-made ternary nanocomposite showed the best separation efficiency, due to the formation of multiple heterojunction structures in the Fe_3O_4@CeO_2@BiOI nanospheres. The combination of Fe_3O_4, CeO_2 and BiOI in the as-made catalyst can provide more photo-generated charge carriers that can improve the photocatalytic activity.

Fig. 4d shows the electrochemical impedance spectroscopy (EIS) of the samples. In EIS analysis, the smaller arc radius confirms that the catalyst has lower electron transfer resistance (Jiang et al. 2019). According to the results,

the arc radius of the as-made Fe_3O_4@CeO_2@BiOI nanocomposite is lower than the pure BiOI and CeO_2, which indicated that the separation and transformation of the photo-generated charge carriers can be enhanced in the ternary nanocomposite. This behavior is a precursor for an enhanced photocatalytic activity for the new nano-catalyst under UVA.

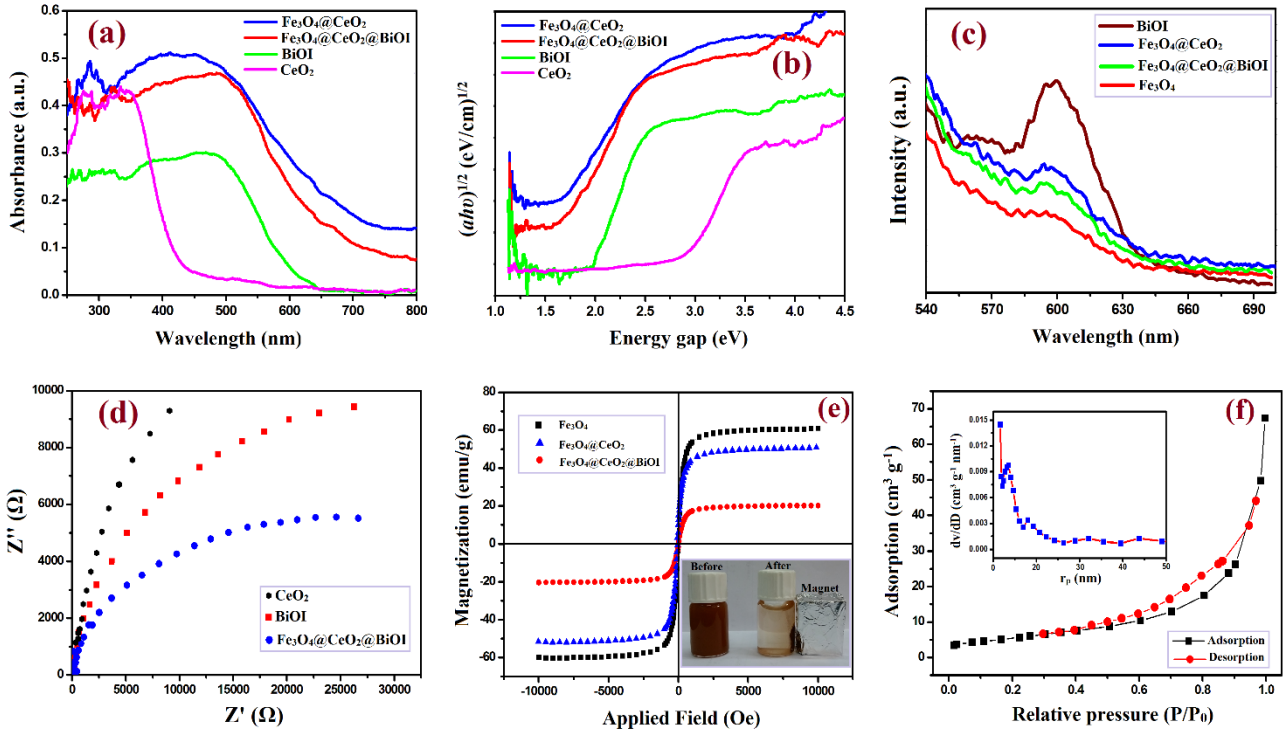

Figure 4. UV-Vis DRS spectra (a), band gap energies (b), PL spectra (c), electrochemical impedance spectroscopy (d), and VSM analysis of as-made samples (e). N_2 adsorption/desorption isotherms of Fe_3O_4@CeO_2@BiOI nanosphere at 77 K (The insert figure shows the BJH plot of this catalyst.) (f).

To investigate the magnetic properties of as-made catalysts, vibrating-sample magnetometry (VSM) analysis was applied. Fig. 4e shows the magnetization curves of Fe_3O_4, Fe_3O_4@CeO_2, and Fe_3O_4@CeO_2@BiOI catalysts. Based on the results, all samples were super-paramagnetic at room temperature (Khavar et al. 2019). The saturated magnetization (*Ms*) values of Fe_3O_4, Fe_3O_4@CeO_2, and Fe_3O_4@CeO_2@BiOI nanocomposite were calculated to be 60.1 emu g^{-1}, 51.2 emu g^{-1}, and 20.2 emu g^{-1}, respectively. The *Ms* value of ternary nanocomposite was lower than the respective of the magnetic NPs, which can confirm the covering of Fe_3O_4 spheres by CeO_2, and BiOI that decrease the magnetic responsiveness. Nevertheless, the ternary nano-photocatalyst maintains significant magnetic

properties, which facilitate its easy separation from the reaction media by using an external magnet, as shown in the insert of Fig. 4e.

The specific surface area and the pore size distribution of the Fe_3O_4@CeO_2@BiOI nanocomposite were studied by measuring the N_2 adsorption/desorption isotherms (Fig. 4f). Due to the presence of a hysteresis loop of the sample at $0 < P/P_0 < 1$, the isotherm of the catalyst can be related to type IV, which is characteristic of the mesoporous materials (Khavar et al. 2019). This result confirmed the pore size distribution obtained from the BJH method (see: insert in Fig. 4f), in which the mesoporous range can be found (10-25 nm). The specific surface area of the Fe_3O_4@CeO_2@BiOI nanocomposite was estimated to be 39.6 m^2 g^{-1}.

3.2. Catalytic activity of the as-synthesized materials in SMX degradation

3.2.1. Performance of SMX photo-degradation assisted by UVA/PMS.

To identify the photo-catalytic performance of the as-made samples in the activation of PMS, the SMX degradation was carried out under different conditions and the obtained results are illustrated in Fig. 5a, b.

Adsorption – PMS Activation (without irradiation): As a first step, Fe_3O_4, BiOI, Fe_3O_4@CeO_2 (hereon: FeCe), and Fe_3O_4@CeO_2@BiOI (hereon: FeCeBi) nanocomposites were used under dark conditions without the addition of PMS. Only 2.75%, 3.40%, and 14.0% of SMX was adsorbed on the surface of Fe_3O_4, FeCe, and BiOI catalysts, respectively. By introducing the BiOI on the surface of the Fe_3O_4@CeO_2 catalyst, adsorption was increased and reached 22.0% over the FeCeBi nanocomposite during the first 15 min of the reaction. In catalytic processes, i.e., in presence of PMS, FeCeBi showed high catalytic activity in SMX degradation in compare with pure BiOI, CeO_2, FeCe, and CeO_2@BiOI (hereon: CeBi) catalyst. The SMX removal (%) was obtained to be 66%, 58%, 55%, 40%, and 25%, over FeCeBi/PMS, CeBi/PMS, FeCe/PMS, CeO_2/PMS, and BiOI/PMS processes, respectively (Fig. 5c). As such, we verify that the presence of different metals in as-made nanocomposite, hence different redox cycles of metal ions, can improve the reaction efficiency (Kohantorabi et al, 2021b).

SMX photolysis – UVA activation of PMS – Photocatalysis (without PMS): PMS activation by UVA light has been previously observed (Ozores-Diez et al., 2020); here, by introducing the light to catalytic system, the reaction

efficiency was enhanced as well. Almost 35% of SMX could be removed from the reaction media in the presence of PMS/UVA process, while this value was 12.5%, and 15% under UVA and PMS alone, respectively (Fig. 5c). So, this result confirmed the activation of PMS under irradiation of UVA in the removal of SMX. Among the as-prepared samples in this study, the FeCeBi nanocomposite showed high photocatalytic activity in SMX degradation under UVA light. The photocatalytic activity of these samples under UVA irradiation was decreased as follows: CeBi (81%) > FeCeBi (79%) > BiOI (53%) > FeCe (40%) > CeO_2 (30%) (Fig. 5c). Due to the formation of the heterojunction structure between CeO_2 and BiOI, the binary and ternary nanocomposites showed considerably high activity in this reaction, which can enhance the recombination of e^-/h^+ pairs. The rate constant value of Fe_3O_4@CeO_2@BiOI/UVA was 0.1045 min^{-1}, while this value was calculated to be 0.051 min^{-1}, 0.033 min^{-1}, and 0.023 min^{-1} for the BiOI/UVA, Fe_3O_4@CeO_2/UVA, and CeO_2/UVA processes, respectively.

Photo-catalytic activation of PMS (Fe_3O_4@CeO_2@BiOI/UVA/PMS): To investigate the PMS activation in the photocatalytic reaction, the SMX degradation was tested over each sample, coupled with UVA and PMS. Based on the results (Fig. 5a, and 5c), by addition of PMS to the photocatalytic reactions, the reaction efficiency was enhanced, and the best performance was obtained for the FeCeBi/UVA/PMS process. The PFO rate constant values were significantly increased in the photocatalytic systems coupled with PMS. This value for FeCeBi/UVA/PMS system (0.2213 min^{-1}) was 4.04, 3.76, and 3.54 times higher than CeO_2/UVA/PMS, BiOI/UVA/PMS, and FeCe/UVA/PMS, respectively. In this way, we evidence that the cycles of Fe(III)/Fe(II), Ce(IV)/Ce(III), and Bi(III)/Bi(V) can accelerate the activation of PMS and enhance the reaction efficiency (eqns. 11-16).

In the presence of the BiOI, not only the activation of PMS was increased due to presence of the Bi(III)/Bi(V) redox cycle, resulting in formation of $SO_4^{\bullet-}$ and $HO^{\bullet}$ (eqns. 15 and 16), but also the photocatalytic efficiency was enhanced via the generation of e^-/h^+ pairs between CeO_2 and BiOI. In addition, the possible generation of $SO_5^{\bullet-}$ can improve the reaction efficiency by the formation of hydroxyl and sulfate radicals (eqns. 17 and 18) (Kohantorabi et al. 2021a). Hence, by the addition of PMS to the reaction, the SMX degradation was enhanced, due to the activation of this oxidant by both UVA irradiation and the photocatalyst.

$$Fe^{3+} + HSO_5^- \longrightarrow Fe^{2+} + SO_5^{\bullet-} + H^+ \qquad k = Not\ found \qquad (11)$$

$$Fe^{2+} + HSO_5^- \longrightarrow Fe^{3+} + SO_4^{\bullet-} + HO^- \qquad k = 3.0 \times 10^4\ M^{-1}s^{-1} \qquad (12)$$

$$Ce^{4+} + HSO_5^- \longrightarrow Ce^{3+} + SO_5^{\bullet -} + H^+ \quad (13)$$

$$Ce^{3+} + HSO_5^- \longrightarrow Ce^{4+} + SO_4^{\bullet -} + HO^- \quad (14)$$

$$Bi^{3+} + 2HSO_5^- \longrightarrow Bi^{5+} + 2SO_4^{\bullet -} + 2HO^- \; and/or \; 2HO^{\bullet} + 2SO_4^{2-} + Bi^{5+} \quad (15)$$

$$Bi^{5+} + 2HSO_5^- \longrightarrow Bi^{3+} + 2SO_5^{\bullet -} + 2H^+ \quad (16)$$

$$SO_5^{\bullet -} + 2H_2O \longrightarrow SO_4^{2-} + 3HO^{\bullet} + H^+ \quad (17)$$

$$2SO_5^{\bullet -} \longrightarrow 2SO_4^{\bullet -} + O_2 \quad (18)$$

It should be noted that the redox potential (E°) of Fe^{3+}/Fe^{2+}, and Ce^{4+}/Ce^{3+} is 0.77 V and 1.44 V, respectively (Xu and Wang, 2012). So, the electron transfer is thermodynamically favorable from Fe^{2+} to Ce^{4+} that can regenerate Ce^{3+} through the equation 19 (Xu and Wang, 2012). Afterwards, Ce^{3+} can react with PMS and produce $SO_4^{\bullet -}$ (eq. 14).

$$Ce^{4+} + Fe^{2+} \longrightarrow Ce^{3+} + Fe^{3+} \quad (19)$$

To better understand the photocatalytic performance of the as-made samples towards SMX degradation, the quantum yield and figure of merit (QY and FoM) parameters were calculated, and the results illustrated in Fig. 5d. According to the obtained results, among the as-prepared samples that used under UVA irradiation for the SMX degradation, the highest QY value 5.02×10^{-4} molecules $photon^{-1}$ was seen for the ternary FeCeBi nanocomposite. In addition, to evaluate the practical efficacy of the reaction system, FoM values were determined by incorporating the four most important performance variables (Fig. 5d). Effective modification of Fe_3O_4 NPs with CeO_2 and BiOI, improved the photocatalytic performance in SMX degradation, due to the activation of PMS. The catalytic performance of FeCeBi catalyst was compared with catalysts used in other AOPs works for the degradation of SMX, and the results are reported in Table 1. According to these results, among the various metal oxide-based catalysts such as $FeVO_4$ (Zhang et al. 2021), Fe_2O_3/MnO_2 (FM) (Guo et al. 2020b), and $CuBi_2O_4$ (Zhang et al. 2020) that have so far been used for SMX degradation under Visible-light (Vis) irradiation, FeCeBi catalyst showed the best activity with the highest value of r_{obs} (2.65 mg/L.min). In all reported systems in literature (Table 1), both radical and non-radical pathways are the dominant mechanisms for degradation of SMX, hence the determination of the pathways in our photo-catalytic process will also be assessed.

Table 1. An overview of the literature on SMX removal by different catalytic systems.

Catalyst (g/L)	[Catalyst] (g/L)	pH	Light source	SMX (mM)	C/O[a] (g/L. mM)	RE (%)	k_{app} (min^{-1})	r_{obs} (mg/L.min)	Reactive species	Ref
FeCeBi	0.1	5.0	UVA	0.05	0.5	97.0% in 15 min	0.221	2.65	$SO_4^{\bullet-}, HO^{\bullet}, O_2^{\bullet-}$	*
$CuO@FeO_x@Fe^0$	1.0	5.7	-	0.04	5.0	86.8% in 10min	0.212	2.12	$SO_4^{\bullet-}, HO^{\bullet}, O_2^{\bullet-}, {}^1O_2$	[He et al. 2020]
$FeCo_2S_4$-CN	0.02	6.5	-	0.02	0.133	91.9% in 15 min	0.151	0.755	$^1O_2$	[Li et al.2020]
$NiCo_2O_4$-EG	0.06	6.3	-	0.02	0.02	100% in 30 min	0.131	0.655	$SO_4^{\bullet-}, HO^{\bullet}, {}^1O_2$	[Xu et al. 2020]
$FeVO_4$	0.5	n.f.	Vis	0.02	1.23	96.6% in 60 min	0.056	0.28	$O_2^{\bullet-}, h^+, {}^1O_2, SO_4^{\bullet-}, HO^{\bullet}$	[Zhang et al. 2021]
FeO_y/S-g-C_3N_4	0.5	3.54	-	0.04	0.625	100% in 90 min	0.06	0.6	$SO_4^{\bullet-}, {}^1O_2$	[Wang et al. 2020b]
Fe_2O_3/MnO_2	0.06	5.7	Vis	0.04	N.F.	90% in 40 min	0.0508	0.508	$SO_4^{\bullet-}, HO^{\bullet}, h^+, {}^1O_2$	[Guo et al. 2020b]
$CuBi_2O_4$	0.5	n.f.	Vis	0.02	N.F.	78% in 60 min	0.0237	0.1185	$SO_4^{\bullet-}, HO^{\bullet}, h^+, {}^1O_2$	[Zhang et al. 2020]
MoS_2/Fe^{2+}	0.3	3.0	-	0.025	4.0	88.5% in 6 min	n.f.	n.f.	$SO_4^{\bullet-}, HO^{\bullet}$	[Wang et al. 2020c]

*a. Catalyst to oxidant ratio, n.f. Not Found, - Without using light, * This work.*

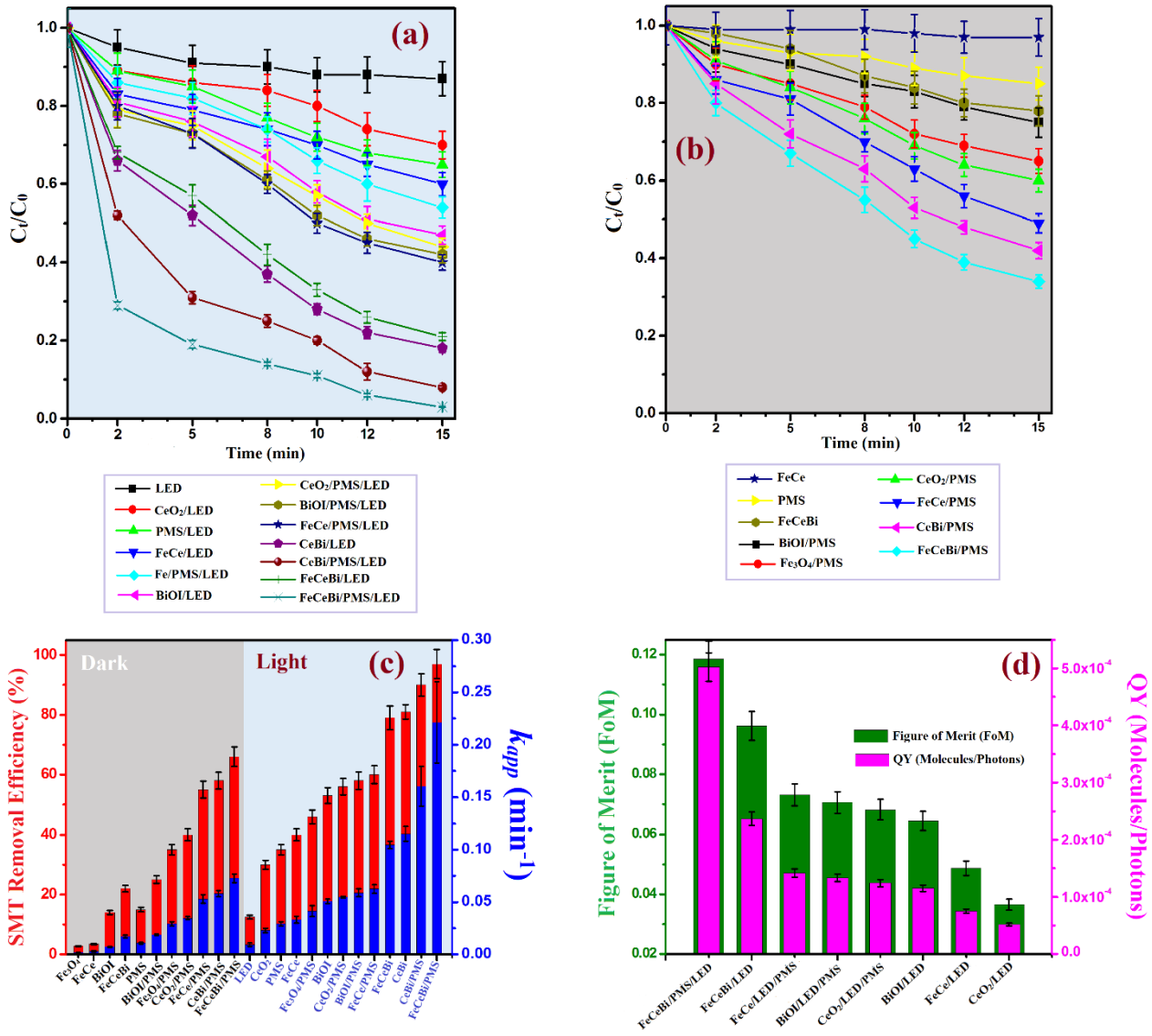

Figure 5. SMX removal efficiency over the different catalytic processes under light irradiation (a), and in the dark (b). The calculated of k_{app} values in these processes (c), quantum yield (QY) and figure of merits (FoM) values for various photocatalytic processes (d). (Reaction conditions: $[SMX]_0$ = 0.05 mM, [PMS] = 0.2 mM, [Catalyst] = 0.1 g/L, reaction time =15 min, under UVA irradiation).

3.2.2. Tweaking the SMX degradation process: effect of the PMS/catalyst ratio

As a first step of this part, the PMS decay was measured at the end of the reaction over the different photocatalytic processes, and the related results are presented in Fig. 6a. The FeCeBi/UVA system can utilize 83.7% of the PMS within 15 min reaction time, while 66.3%, 43.3%, and 38.1% were obtained for the FeCe/UVA, CeO_2/UVA, and

BiOI/UVA processes, respectively. Meanwhile, only 16.8% of PMS was used in the presence of UVA alone. These results confirmed the synergistic effect of the as-made ternary FeCeBi nanocomposite in PMS activation. Based on the obtained results, the concentration of PMS in this reaction was enough (no reactant limitation). So, the influence of FeCeBi catalyst dosage between 0.02 g/L to 0.14 g/L was studied in the photocatalytic PMS activation, while the PMS concentration was kept constant (0.2 mM). Fig. 6b shows the effect of catalyst:PMS ratio on SMX removal efficiency. By increasing the catalyst dosage from 0.02 g/L to 0.1 g/L, the reaction efficiency was increased. Due to the presence of more active catalytic sites, and the generation more reactive species, higher removal of SMX was observed at high catalyst dosage. However, increasing the ratio from 0.5 g/L. mM to 0.7 g/L. mM the removal efficiency was unchanged, indicating a self-inhibition process (i.e., light penetration). To better understand the influence of the catalyst:PMS dosage on SMX removal, the k_{app} values of reaction were calculated, and the corresponding results illustrated in Fig. 6b. The reaction rate constant values increased from 0.054 min^{-1} to 0. 256 min^{-1} when the catalyst:PMS ratio was 0.1 g/L. mM and 0.6 g/L. mM, respectively. Meanwhile, when this ratio reached to 0.7 g/L. mM this value was slightly decreased. Based on the above results, 0.5 g/L. mM was selected as optimum ratio of catalyst:PMS for the SMX degradation under UVA light. Consequently, 0.5 g/L. mM ([catalyst] = 0.1 g/L, and [PMS] = 0.2 mM) were selected as the optimum catalyst:PMS levels for the removal of SMX under UVA irradiation.

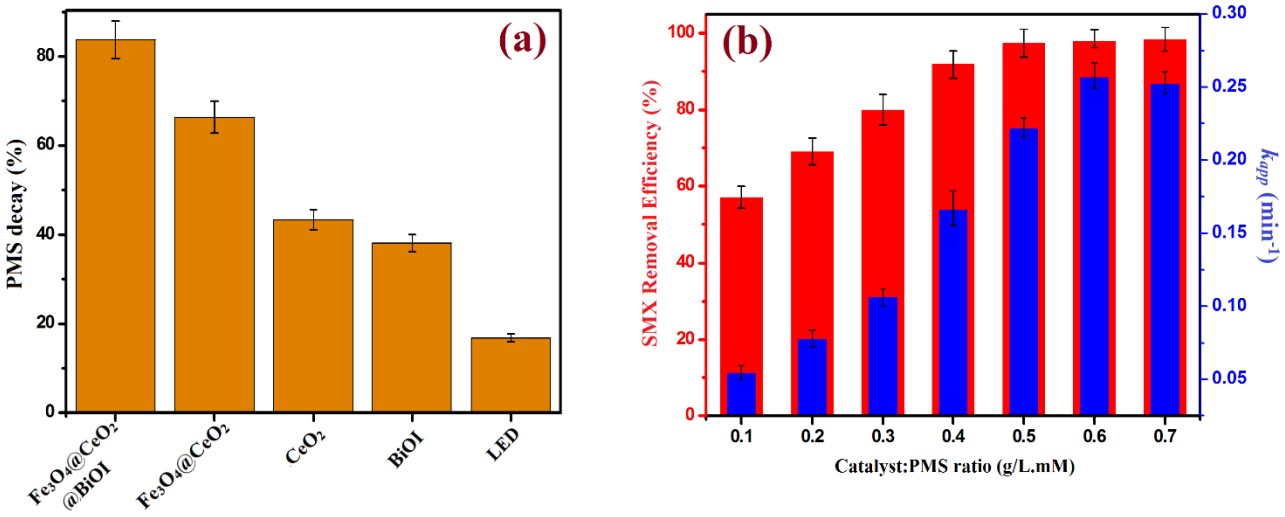

Figure 6. PMS concentration after different photocatalytic processes (a); the effect of catalyst:PMS dosage on SMX degradation and PFO rate constant values of reaction in different catalyst:PMS dosages (b) (Reaction conditions: [SMX] = 0.05 mM, [PMS] = 0.2 mM, solution pH = 5.0, and reaction time = 15 min).

3.2.3. Effect of the initial solution pH

Initial solution pH is an important parameter in catalytic activation of PMS. Some of the factors, including dissociation of PMS, surface charge of catalyst (active sites), and properties of organic pollutants, will be influenced by the solution pH (Lu et al. 2019). The influence of initial solution pH on SMX degradation under catalyst/UVA/PMS system was investigated, and the results are shown in Fig. 7a. Due to the presence of cationic, zwitterionic, and anionic forms of SMX in the different pH conditions, pH is a critical parameter in this reaction (Yang et al. 2019). The pK_a values of SMX are 1.8, and 5.7 which indicated SMX molecules are neutral in the solution with the pH ranges of 1.8-5.7. Based on these results, at pH < 1.8 the cationic forms of SMX (SMX^+) are dominant while the anionic forms (SMX^-) are dominant species at pH > 5.7.

Following, the surface charge of catalyst can affect the reaction efficiency at various pH values. The pH_{zpc} of FeCeBi catalyst was calculated to be around 6.5, which indicated the surface of as-made nanocomposite was positively charged at pH < 6.5, and negatively charged at pH > 6.5. The SMX was nearly completely degraded (97.0%) at pH = 5.0 after 15 min. Under acidic conditions (pH = 3.0), the reaction efficiency was slightly decreased and reached to be 75.9%. Hence, due to negative surface charge of nanocomposite and presence of anionic forms of SMX at basic conditions, the interaction between SMX and the nanocomposite was dropped which caused the low reaction efficiency.

In addition, the solution pH could affect PMS activation during the reaction. According to the pK_a value of PMS ($pK_{a2} = 9.4$), at pH below 9.4 HSO_5^- ions are vital species during the reaction, meanwhile at pH values over 9.4, SO_5^{2-} would dominate the reaction. This can be related to presence of H^+ in reaction media, which decrease the activation of PMS by the formation of H-bonds between H^+, and O─O group on HSO_5^-. However, based on the results, the lowest reaction efficiency was obtained at pH = 11 (68.3%) for SMX degradation. At pH > pH_{zpc} surface charge of catalyst is negative that can reduce the interaction between PMS, and the surface of catalyst. Furthermore, at high pH values, hydroxyl ions can react with CO_2, which is an intermediate degradation product, and produce HCO_3^- and/or CO_3^{2-} ions. These ions can scavenge the $SO_4^{\bullet-}$, and $HO^\bullet$ and decrease the reaction efficiency (see Section. 3.2.4) (Yang et al. 2019). To better understand the influence of the initial solution pH on SMX degradation, the PFO rate constant value of the reaction was calculated at pH ranges (3.0-11), and the obtained results illustrated

in Fig. 7b. The highest rate constant value was obtained at pH = 5.0 (0.2213 min^{-1}) which was approximately 2.2, 1.64, 2.1, and 2.8 times higher than the value which calculated at pHs 3.0, 7.0, 9.0, and 11, respectively. Most likely, pH = 5.0 expresses a point where the favorable conditions meet, namely positively charged catalyst with an anionic form of SMX and the HSO_5^- form of PMS.

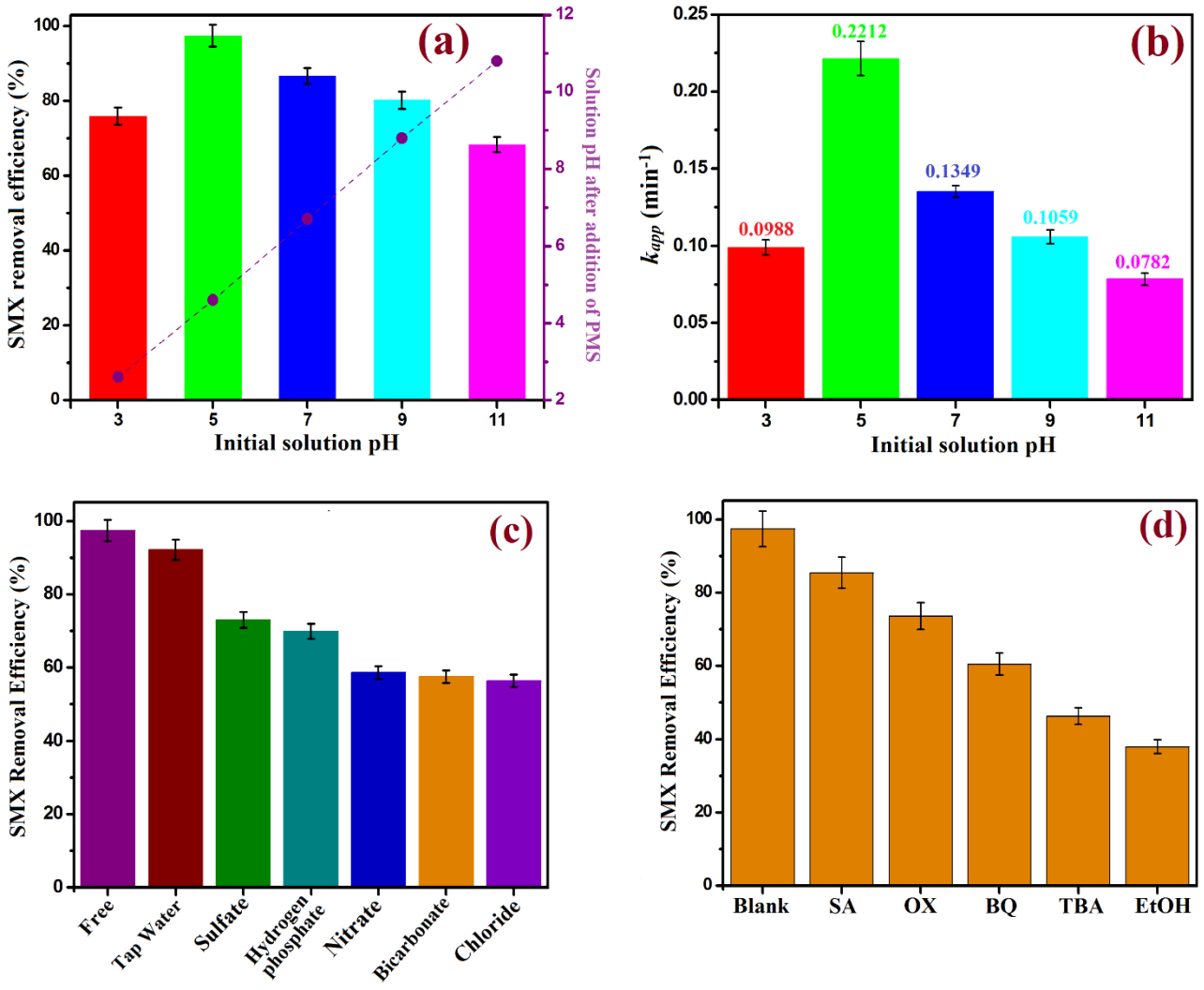

Figure 7. (a) Effect of the initial solution pH on SMX degradation, (b) the PFO rate constant values of reaction at different pH values. (c) Effect of different ions, and (d) different scavengers on SMX degradation in FeCeBi/UVA/PMS process (Reaction conditions: $[SMX]_0$ = 0.05 mM, [PMS] = 0.2 mM, [Catalyst] = 0.1 g/L, [scavenger] = 10 mM).

3.2.4. Effect of water matrix composition in SMX photocatalytic degradation efficacy

In order to clarify the role of various ions in solution reaction, the influence of different ions, including chloride (Cl^-), hydrogen phosphate (HPO_4^{2-}), nitrate (NO_3^-), bicarbonate (HCO_3^-), sulfate (SO_4^{2-}), and tap water (as a simulation of a mixture), was investigated in SMX degradation under FeCeBi/PMS/UVA process (Fig. 7c). The concentration of all ions was selected 100 mg/L during the reaction, and the other reaction conditions were constant. When the Cl^- ions were added into the reaction, the lowest efficiency of the FeCeBi nanocomposite toward degradation of SMX was obtained (56.3%). Due to presence of PMS, and the reaction with Cl^-, different radical and oxidative species including $Cl^{\bullet}$, $Cl_2^{\bullet-}$, $HOCl^{\bullet-}$, Cl_2, and HOCl can be generated (eqns. 20-26). These species have lower oxidation potential and the PPRI are transformed to less potent and more selective ones. In comparison with $SO_4^{\bullet-}$ ($E^{\circ}(SO_4^{\bullet-}/SO_4^{2-}) = 2.5 - 3.1\ V$), $Cl^{\bullet}$ ($E^{\circ}\ (Cl^{\bullet}/Cl^-) = 2.4\ V$) and $Cl_2^{\bullet-}$ ($E^{\circ}\ (Cl_2^{\bullet-}/2Cl^-) = 2.1\ V$) have lower redox potential that can reduce the oxidation efficiency (Hong et al. 2020). In addition, the existence of Cl^- can react with photo-generated hole (h^+) and produce the $Cl^{\bullet}$ (eq. 26). All the newly generated radicals, which are formed by the following reactions, result in lower activity for the degradation of SMX.

$$Cl^- + SO_4^{\bullet-} \longrightarrow Cl^{\bullet} + SO_4^{2-} \qquad k_{Cl^- + SO_4^{\bullet-}} = 2.8 \times 10^8\ M^{-1}s^{-1} \qquad (20)$$

$$Cl^{\bullet} + Cl^- \longrightarrow Cl_2^{\bullet-} \qquad k_{Cl^- + Cl^{\bullet}} = 8.0 \times 10^9\ M^{-1}s^{-1} \qquad (21)$$

$$HO^{\bullet} + Cl^- \longrightarrow HOCl^{\bullet-} \qquad (22)$$

$$HO^{\bullet} + Cl^- + O_2 \longrightarrow HOCl + O_2^{\bullet-} \qquad (23)$$

$$HOCl^{\bullet-} + H^+ \longrightarrow Cl^{\bullet} + H_2O \qquad (24)$$

$$HOCl^{\bullet-} + Cl^- \longrightarrow Cl_2{}^{\bullet-} + OH^- \qquad (25)$$

$$h_{VB}^+ + Cl^- \longrightarrow Cl^{\bullet} \qquad (26)$$

Among the inorganic ions which exist in natural waters, bicarbonate is a typical species with mean concentration around 264 mg L^{-1} or 4.3 mM (Zhai et al. 2019). It was found that by addition of HCO_3^- ions, the reaction efficiency decreased from 97.0% to 57.48%. This behavior can be related to reaction between HCO_3^- and/or CO_3^{2-} with photo-generated species such as h^+ and $HO^{\bullet}$, which produce $CO_3^{\bullet-}$ radicals having lower activity on degradation process (Guo et al. 2020c), in a similar fashion to Cl-based radicals. Moreover, the presence of HCO_3^- ions can scavenge $SO_4^{\bullet-}$ and $HO^{\bullet}$, which causes a decrease in SMX degradation efficiency (eqns. 27 and 28). This ion can react with

both sulfate and hydroxyl radicals at a rate constant of 1.6×10^6 M^{-1} s^{-1}, and 8.5×10^6 M^{-1} s^{-1}, respectively. Moreover, the presence of bicarbonate can change the pH solution to basic and affect the reaction efficiency (Hong et al. 2020). By addition of HCO_3^- into the reaction solution, the solution pH was increased and remained at 7.0-9.0 due to dynamic equilibrium (Wang et al. 2020d) that can decrease the reaction efficiency.

$$HCO_3^- + SO_4^{\bullet -} \longrightarrow HCO_3^{\bullet -} + SO_4^{2-} \qquad k_{HCO_3^-/SO_4^{\bullet -}} = 1.6 \times 10^6\ M^{-1}s^{-1} \tag{27}$$

$$HCO_3^- + HO^\bullet \longrightarrow CO_3^{\bullet -} + H_2O \qquad k_{HCO_3^-/HO^\bullet} = 8.5 \times 10^6\ M^{-1}s^{-1} \tag{28}$$

From Fig. 7c, the presence of NO_3^- in the reaction can affect photo-oxidation and the photocatalytic process via light absorption (Moradi et al. 2020). With NO_3^- present in the reaction solution, the reaction efficiency was decreased to 58.60%. NO_3^- would be converted to the $NO_3^\bullet$, and $NO_2^\bullet$ with lower redox potential (2.3 V and 1.03 V, respectively) by the trapping of $SO_4^{\bullet -}$, and $HO^\bullet$ (eqns. 29-32), which outperform the excitation of nitrate by light that results in $HO^\bullet$ production (Rommozzi et al. 2020). So, the presence of NO_3^- ions can decrease the reaction efficiency.

$$NO_3^- + SO_4^{\bullet -} \longrightarrow NO_3^\bullet + SO_4^{2-} \qquad k = 5.0 - 210 \times 10^4\ M^{-1}s^{-1} \tag{29}$$

$$NO_3^- + HO^\bullet \longrightarrow NO_3^\bullet + HO^- \qquad k = Not\ found \tag{30}$$

$$NO_3^\bullet + H_2O + e^- \longrightarrow NO_2^\bullet + 2HO^- \qquad k = 8.6 - 11 \times 10^9\ M^{-1}s^{-1} \tag{31}$$

$$NO_3^- + H_2O + hv \longrightarrow NO_2^\bullet + HO^- + HO^\bullet \tag{32}$$

As it can be seen from the results, the presence of Cl^-, HCO_3^-, and NO_3^- showed a similar, inhibiting behavior on this reaction, and SMX degradation (%) was calculated to be 56.30%, 57.48%, and 58.60% in the presence of the aforementioned ions, respectively.

$HPO_4^{2-}$is another important scavenger for sulfate and hydroxyl radicals, although its concentration has a vital role in degradation efficiency. In this study, at the selected concentration, low efficiency was obtained, due to scavenging of $HO^\bullet$, and $SO_4^{\bullet -}$ which can produce other radicals ($HPO_4^{\bullet -}$) with low activity (eqns. 33 and 34). The reaction rate constant between HPO_4^{2-} and $SO_4^{\bullet -}$ ($1.2\text{-}1.6 \times 10^6$ min^{-1}) is 100 times higher than $HO^\bullet$ ($2.0\text{-}15 \times 10^4$ min^{-1}). So, the

hydrogen phosphate ion is an effective quencher for $SO_4^{\bullet-}$ compared with $HO^{\bullet}$. Also, the HPO_4^{2-} can generate an inner-sphere complex with the surface of metal catalyst that effect on the SMX removal efficiency (Hong et al. 2020).

$$HPO_4^{2-} + SO_4^{\bullet-} \longrightarrow HPO_4^{\bullet-} + SO_4^{2-} \quad (33)$$

$$HPO_4^{2-} + HO^{\bullet} \longrightarrow HPO_4^{\bullet-} + HO^{-} \quad (34)$$

Finally, the negative effect of the presence of SO_4^{2-} ions in this reaction, can be attributed to the scavenging of $HO^{\bullet}$ radicals, and less of $SO_4^{\bullet-}$ (eqns. 35 and 36). It should be noted that, the equation 36 can occur only at pH < 3.0, in which $SO_4^{\bullet-}$ can be formed (Rommozzi et al. 2020).

$$HSO_4^{-} + HO^{\bullet} \longrightarrow SO_4^{\bullet-} + HO^{-} \qquad pH < 3.0 \quad (35)$$

$$SO_4^{\bullet-} + SO_4^{2-} \longrightarrow S_2O_8^{2-} + e_{aq}^{-} \quad (36)$$

3.3. Photo-degradation mechanism of SMX and the pathways to its elimination

3.3.1. Reactive species identification by scavenger tests

For the assessment of the PPRI generated during the photo-degradation of SMX by the FeCeBi/PMS/UVA process, radical trapping experiments were performed. Different kinds of scavengers including benzoquinone (BQ), ethanol (EtOH), tert-butanol (TBA), sodium azide (SA), and oxalate (OX) were applied as $O_2^{\bullet-}$, both $SO_4^{\bullet-}$ and $HO^{\bullet}$ simultaneous trap, $HO^{\bullet}$, $^1O_2$, and photo-generated h^+ sequesters, respectively. Fig. 7d displays the reaction efficiency of SMX removal in the presence of various scavengers. The SMX degradation efficiency was decreased from 97.0% to 85.4%, 73.6%, 60.5%, 46.3%, and 38% after adding the SA, OX, BQ, TBA, and EtOH, respectively. EtOH is a scavenger for both $SO_4^{\bullet-}$, and $HO^{\bullet}$ in which the rate constant with $SO_4^{\bullet-}$ and $HO^{\bullet}$ is 1.6-7.7 × 10^7 M^{-1} s^{-1}, and 1.2-2.8 × 10^9 M^{-1} s^{-1}, respectively (Kohantorabi et al. 2021b). Meanwhile, TBA, which does not have *a*-hydrogen in its molecule can react with $HO^{\bullet}$ ((3.6-7.6) × 10^8 M^{-1} s^{-1}) 1000 times higher than $SO_4^{\bullet-}$ ((4.0-9.1) × 10^5 M^{-1} s^{-1}), hence it can be used as a strong scavenger for only $HO^{\bullet}$ (Kohantorabi et al. 2021b). According to the obtained results, the lowest reaction efficiency was observed in the presence of EtOH, and TBA, which indicated

that $SO_4^{\bullet-}$ and $HO^{\bullet}$ played critical role in reaction efficiency. By addition of BQ as $O_2^{\bullet-}$ scavenger into the reaction ($k_{O_2^{\bullet-}}$ = 0.9-1.0 × 10^9 min^{-1}), the removal efficiency was decreased and reached to 60.5%, which confirmed the role of $O_2^{\bullet-}$ in this reaction. To assess the direct oxidative photocatalytic activity of the as-made nanocomposite under UVA light irradiation, OX was applied for trapping of photo-generated h^+, with only minimal effect observed. This effect was less pronounced when SA was used, indicating that $^1O_2$ has a minor role in SMX degradation through FeCeBi/UVA/PMS process. Overall, the degradation efficiency was inhibited in the order of EtOH > TBA > BQ > OX > SA (Fig. 7d), and a dominant radical-induced SMX degradation is proposed.

In FeCeBi/UVA/PMS system two main pathways contributed to the degradation of SMX, namely: i) catalytic activation of PMS by the redox cycles of metal ions in the as-made catalyst, and ii) photocatalytic activity of the ternary FeCeBi nanocomposite, which not only can enhance the catalytic activity by the formation of photo-generated e^-/h^+ pairs, but also accelerate the activation of PMS under light. The photo-generated electron (e^-) in the conduction band of CeO_2 can react with dissolved oxygen and produce $O_2^{\bullet-}$, which in turn can contribute in SMX degradation (Hu et al. 2019). Also, some authors have proposed that with the reaction between PMS and $O_2^{\bullet-}$, $SO_4^{\bullet-}$ and $HO^{\bullet}$ can be obtained, which can enhance the reaction efficiency (eq. 42) (Li et al. 2017). Hence, the formation of a heterojunction structure between CeO_2 and BiOI that can facilitate the separation rate of electron/holes, promoting the reaction efficiency of SMX degradation.

3.3.2. Analysis of the plausible SMX degradation mechanism

Based on the above results, and related works in literature, a plausible mechanism for the photocatalytic degradation of SMX over the FeCeBi/UVA/PMS process was proposed and illustrated in Fig. 8. In this process, three reactions played a critical role in photocatalytic performance, and PMS activation. During the SMX oxidation, the Bi^{3+}/Bi^{5+} cycle can activate PMS and generate $SO_4^{\bullet-}$, $HO^{\bullet}$, and $SO_5^{\bullet-}$ in the reaction cycle. The observed peaks in the XPS analysis of the optimum catalyst confirmed the presence of Bi^{3+} in the as-made nanocomposite that can activate PMS (Fig. 8). Moreover, similar activity was observed for the redox cycles of Fe^{2+}/Fe^{3+}, and Ce^{4+}/Ce^{3+} that can participate in activation of PMS, and then formation of more reactive species. According to the semi-empirical equation (eq. 37), based on the Mulliken electronegativity theory, the conduction band potential (CB), and valence

band potential (VB) of CeO_2 and BiOI were calculated by the following equations (eqns. 37 and 38) (Khavar et al. 2019):

$$E_{VB} = X - E_e + 0.5E_g \quad (37)$$

$$E_{CB} = E_{VB} - E_g \quad (38)$$

In which, E_g, E_e, and X are the band gap energy, the energy of free electrons on the hydrogen scale (4.5 eV), and the absolute electronegativity of the constituent atoms. Based on UV-Vis DRS spectra (Fig. 4b), the E_g values of CeO_2 and BiOI were calculated to be 2.72 eV, and 1.92 eV, respectively. The calculated VB potential for CeO_2, and BiOI were estimated to be 2.34 eV, and 2.40 eV, respectively. Hence, the CB values of them were obtained to be -0.38 eV, and 0.48 eV, respectively. Under light irradiation, the photocatalyst can absorb the photon and generate the e^-/h^+ pairs (eq. 39). The CB of CeO_2 is more negative than the CB of BiOI, and the electrons can be transferred from the CB of CeO_2 to the CB of BiOI, to create the electron center. Moreover, the VB potential of BiOI is more positive than VB edge of CeO_2, hence the photo-generated holes can be transferred to VB edge of CeO_2. The photo-generated e^- can react with HSO_5^- and generate $SO_4^{\bullet -}$ and $HO^\bullet$ (eq. 40). Based on the standard reduction potential of $HO^\bullet/H_2O$ (2.27 eV) or $HO^\bullet/HO^-$ (2.38 eV) (Liu et al. 2017), the photo-generated holes in VB of CeO_2, and BiOI cannot oxidize H_2O or HO^- into the $HO^\bullet$. Instead, the h^+ can react directly with SMX molecules and enhance the degradation efficiency (eq. 43), albeit in low rates. Moreover, the CB of CeO_2 is more negative than potential of $O_2/O_2^{\bullet -}$ (-0.33 eV) (Salari and Kohantorabi 2020). Hence, the oxygen molecules can be transformed to $O_2^{\bullet -}$, and react with SMX to produce the degradation products (eq. 41).

$$Fe_3O_4@CeO_2@BiOI + hv \longrightarrow Fe_3O_4@CeO_2@BiOI\ (h_{VB}^+ + e_{CB}^-) \quad (39)$$

$$e_{CB}^- + HSO_5^- \longrightarrow HO^- + SO_4^{\bullet -} or\ HO^\bullet + SO_4^{2-} \quad (40)$$

$$O_2 + e_{CB}^- \longrightarrow O_2^{\bullet -} \quad (41)$$

$$HSO_5^- + O_2^{\bullet -} \longrightarrow SO_4^{\bullet -} + HO^- + O_2 \quad (42)$$

$$SO_4^{\bullet -}/HO^\bullet/O_2^{\bullet -}/h_{VB}^+ + SMX \longrightarrow Degradation\ products\ and\ Intermediates \quad (43)$$

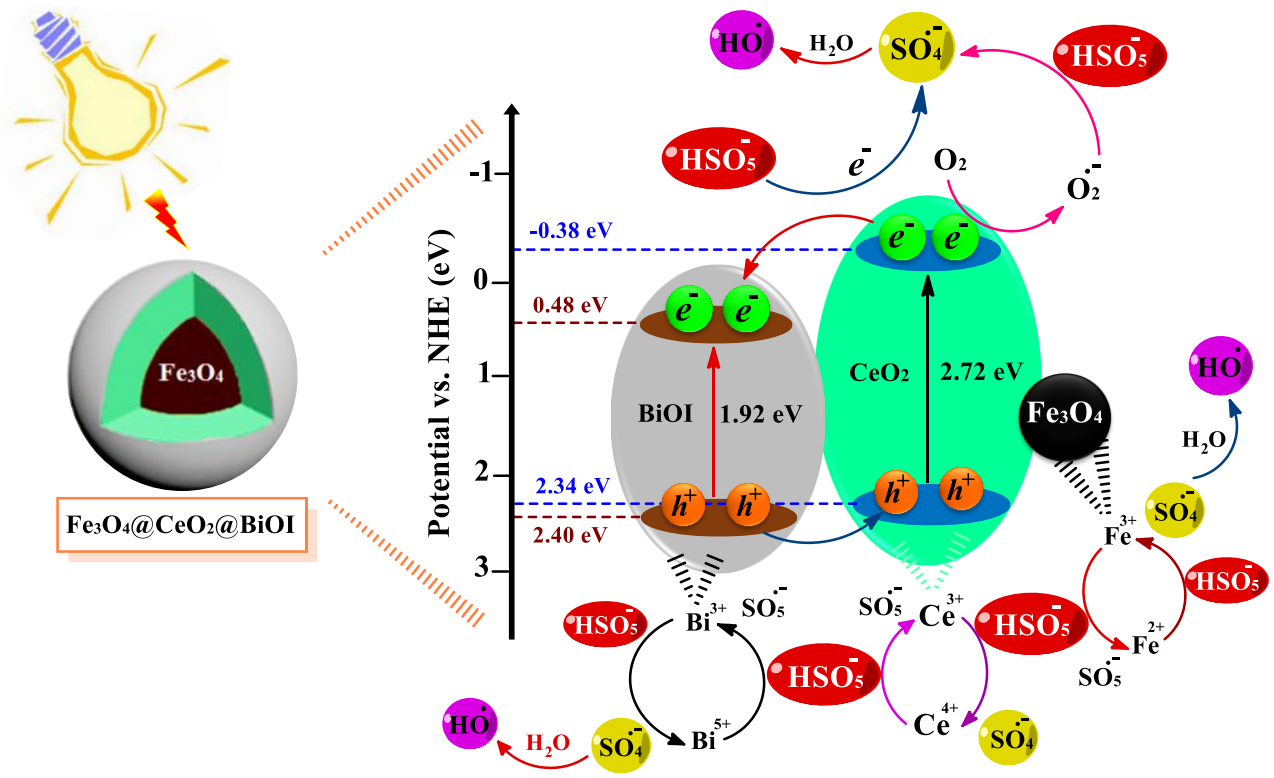

Figure 8. A proposition for the integrated SMX degradation mechanism using the Fe_3O_4@CeO_2@BiOI/PMS nanospheres under UVA light.

3.3.3. Catalyst reusability and stability: ion leaching measurements.

To investigate the catalytic stability of as-made nanocomposite in SMX degradation, the FeCeBi catalyst was tested in four consecutive catalytic cycles under the same reaction conditions. As can be seen from the obtained results (Fig. 9a), no significant change was observed within four catalytic cycles; 95% removal efficiency was obtained during 15 min in 4th catalytic run. These results indicated that the as-made catalyst is an effective and reusable catalysts. Moreover, the leaching amounts of Fe, Ce, and Bi during these four consecutive cycles was evaluated and the results illustrated in Fig. 9b. The concentration of Fe, and Bi increased by the number of FeCeBi reuse cycles. The concentration of cerium (0.08 mg/L) was negligible over the 4 runs. The highest metal leaching is related to the BiOI in as-prepared catalyst, although this value was low in absolute values (0.14 mg/L). According to the ICP results, the as-made ternary nanocomposite is highly stable, since only 0.32% of all metals was released into the solution during the reaction. In addition, based on Chinese standard values of Fe^{2+} (0.3 mg/L) in drinking water

(Kohantorabi et al. 2020), the iron leaching amount from the as-made nanocomposite was low, which is favorable for the stability of catalyst, and for the environment. Fig. 9c shows the XRD patterns of pristine and reused catalysts (after four runs). Based on the results, all characteristic peaks related to Fe_3O_4, CeO_2, and BiOI were observed in XRD pattern of the reused catalyst that confirmed the high structure stability of FeCeBi nanocomposite in catalytic cycles. For a precise estimation of the chemical states of elements in the recovered catalyst, the XPS analysis was applied for the reused catalyst, and the results are depicted in Fig. 3. The XPS results illustrate that the oxidation states of Fe, Ce, and Bi remain constant after reused cycles with a slight shift of binding energies. Based on the results, the high chemical stability of the as-made FeCeBi catalyst was confirmed, showing potential to be applied in water treatment applications.

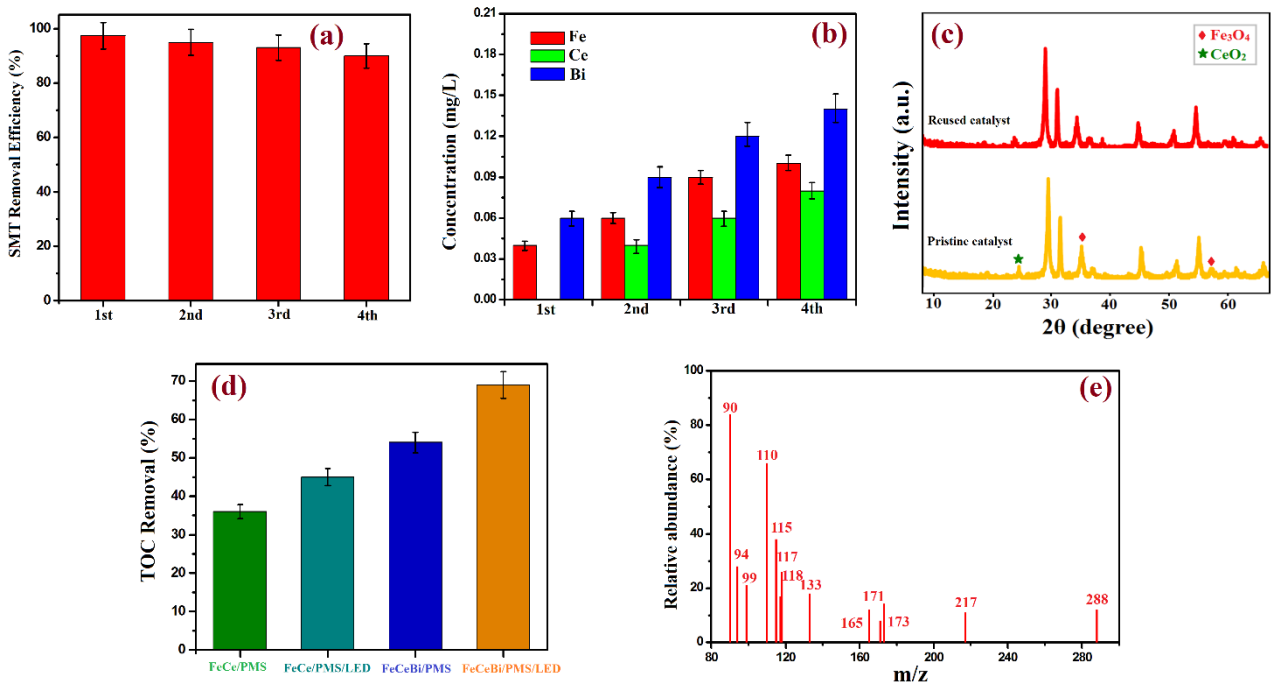

Figure 9. SMX removal efficiency in repetitive catalytic cycles (a), ICP-AES analysis of resultant solution in the various catalytic cycles (b), XRD patterns of pristine and reused Fe_3O_4@CeO_2@BiOI catalyst (c), TOC removal of SMX solutions under different catalytic processes (d), and Mass spectra of SMX degradation in FeCeBi/UVA/PMS process after 60 min of reaction (e). (Reaction condition: $[SMX]_0$ = 0.05 mM, [catalyst] = 0.1 g/L, [PMS] = 0.2 mM, and pH = 5.0, under UVA).

3.3.4. Investigation of the SMX degradation pathway by LC-MS analysis

To study the by-products generated during the degradation of SMX over the FeCeBi nanocomposite coupled with PMS/UVA, LC-MS analysis during the process was applied (Fig. 9e), and the degradation mechanism was proposed based on the detected intermediates (Fig. 10). Based on the previously reported scavenger experiments, reactive species such as $O_2^{\bullet-}$, $SO_4^{\bullet-}$, $HO^{\bullet}$, and less h^+, were mainly involved in SMX degradation and generation of transformation products (TPs). According to the detected TPs along with the fragment's *m/z* ratio, three possible pathways were proposed in the degradation mechanism of SMX over FeCeBi/UVA/PMS system. One mechanism was initiated from the destruction of S-N bond in SMX molecule by radical attack that can produce the 3-amino-5-methylisoxazole (*m/z*=99), and sulfinilic acid (*m/z*=173) (Wang et al. 2020b). Another pathway was started by the destruction of the S-C bond, and 3-amino-5-methylisoxazole (*m/z*=99) and aniline (*m/z*=94) were obtained. By the destruction of C-N bond in the SMX structure, sulfanilamide intermediate with *m/z*=171 was obtained (Yazdanbakhsh et al. 2020). This intermediated can be attacked by $HO^{\bullet}$ and produce 2, 4-dinitrobenzene-sulfinic acid (*m/z*=217) and then converted to the phenylsulfinic acid (*m/z*=165). In the proposed pathway, a TP with *m/z*=288 as di-hydroxylated SMX can be formed through the electrophilic addition on the isoxazole ring by $HO^{\bullet}$, and $SO_4^{\bullet-}$ (Wang et al. 2020c). This intermediate was also reported in other systems such as UVA/PMS, UV/H_2O_2, $CuFe_2O_4$/hydroxylamine/PMS, and MoS_2/Fe^{2+}/PMS (Wang et al. 2020c; Yang et al. 2017). The generated intermediate (*m/z*=288) can be transformed to one with *m/z*=133 via $HO^{\bullet}$ substitution, and then to *m/z*=117 by the ring-opening reaction (Wang et al. 2020c). The formation of low-molecular weight intermediates indicated the continuous attack of $HO^{\bullet}$ that can lead to ring opening and finally formation of small aliphatic acid compounds, CO_2, and H_2O.

According to the TOC measurements (Fig. 9d), when the FeCeBi nanocomposite was used in SMX degradation coupled with UVA/PMS, the TOC removal value (69%) was enhanced compared with FeCeBi/PMS (54%), FeCe/UVA/PMS (45%), and FeCe/PMS (36%) during 60 min of reaction. These results confirmed the high mineralization of SMX during the reaction and then generation of low-molecular weight compounds at the end of the photocatalytic reaction.

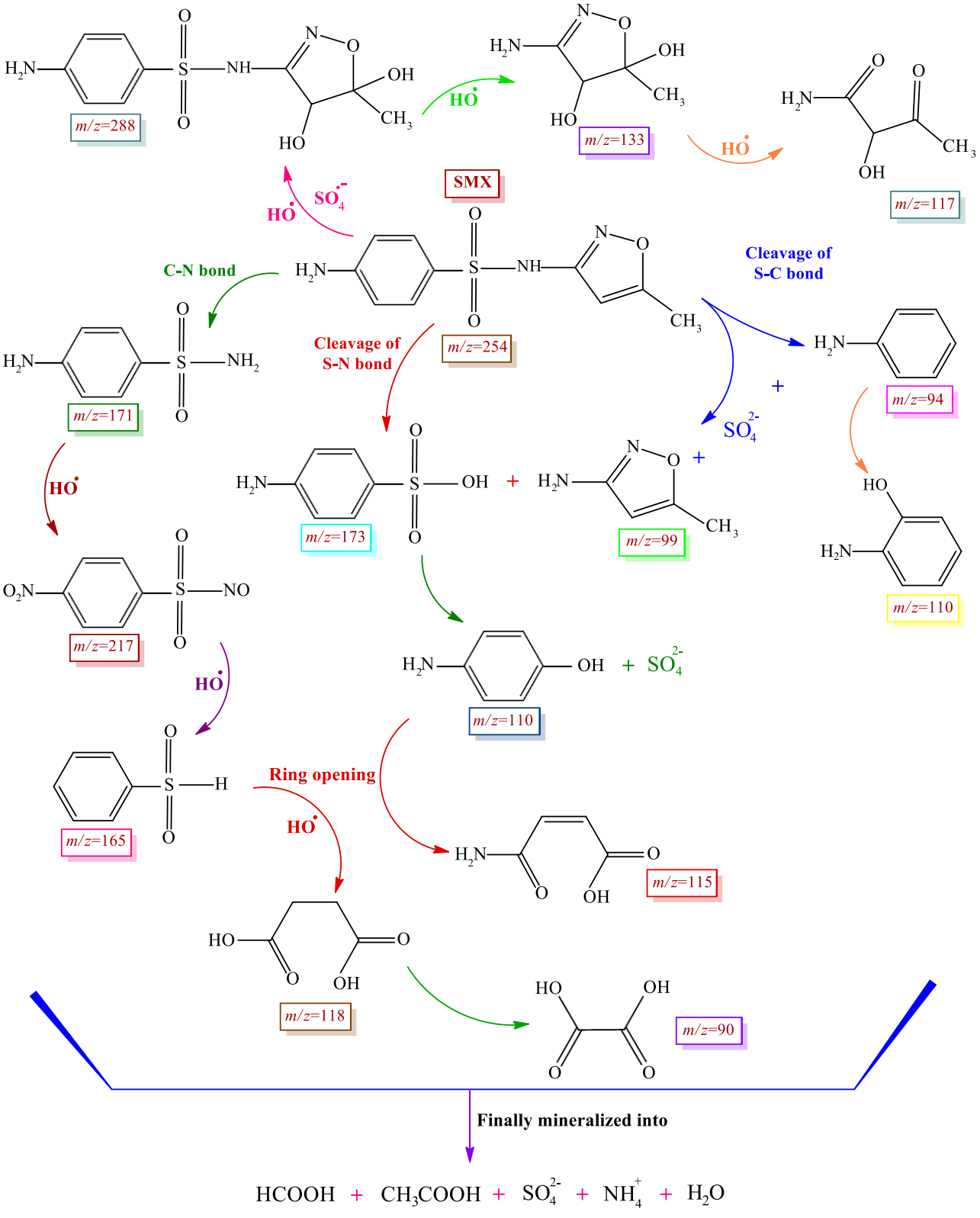

Figure 10. The proposed pathway of SMX degradation over the Fe_3O_4@CeO_2@BiOI/UVA/PMS process (Reaction conditions: [SMX] = 0.05 mM, [PMS] = 0.2 mM, [catalyst] = 0.1 g/L, Solution pH = 5.0, and Reaction time = 60 min).

4. Conclusions

In this study, a novel magnetic Fe_3O_4@CeO_2@BiOI nanocomposite was successfully synthesized by a simple hydrothermal method, with the intention of creating an effective photocatalyst for PMS activation and its use in antibiotics elimination. The as-made photocatalyst showed high catalytic activity in the activation of PMS under UVA-LED for the degradation of SMX. The results demonstrated that the Fe_3O_4@CeO_2@BiOI/UVA/PMS system could degrade 97% of SMX in 15 min at 0.2 mM of PMS, 0.1 g/L of catalyst, and pH=5.0 that was much higher than other catalytic systems including Fe_3O_4@CeO_2/UVA/PMS (60%), CeO_2/UVA/PMS (56%), and BiOI/UVA/PMS (58%). Among the different inorganic ions that could possibly be encountered in water, Cl^-, HCO_3^-, and NO_3^- has significant inhibition, albeit in high concentrations due to the high reaction potential with generated reactive species and their transformation to less oxidative ones.

Additionally, based on the free-radical trapping experiments, $HO^\bullet$, $SO_4^{\bullet-}$ and $O_2^{\bullet-}$ played the dominant role in degradation of SMX over photocatalytic process coupled with PMS. The excellent performance of Fe_3O_4@CeO_2@BiOI/UVA/PMS system for the degradation of SMX can be related to the formation of heterojunction structure between CeO_2 and BiOI, which can promote the transfer and separation of the photo-generated e^-/h^+ pairs. Moreover, by addition of PMS and formation of $SO_4^{\bullet-}$ and $HO^\bullet$ the efficiency of SMX degradation was promoted. High stability and reusability of the as-prepared catalyst was confirmed by consecutive catalytic cycles and the degradation pathway of SMX was elucidated by using the LC/MS analysis; all results combined confirmed the dominant radical pathways.

Overall, the high mineralization degree and the quick removal of SMX by a catalyst with excellent reusability and stability, indicated that coupling this catalyst with PMS and UVA light has a high potential for effective SMX elimination applications.

5. Acknowledgments

This work was technically and financially supported by the Tarbiat Modares University, Iran, under the Research Group grant No. IG-39801. Stefanos Giannakis would like to acknowledge the Spanish Ministry of Science, Innovation and Universities (MICIU) for the Ramón y Cajal Fellowship (RYC2018-024033-I).

6. References

Huang, Z., Dai, X., Huang, Z., Wang, T., Cui, L., Ye, J., Wu, P., 2019. Simultaneous and efficient photocatalytic reduction of Cr(VI) and oxidation of trace sulfamethoxazole under LED light by rGO@Cu_2O/$BiVO_4$ p-n heterojunction composite. *Chemosphere*, 221, 824-833. https://doi.org/10.1016/j.chemosphere.2019.01.087.

Yazdanbakhsh, A., Eslami, A., Massoudinejad, M., Avazpour, M., 2020. Enhanced degradation of sulfamethoxazole antibiotic from aqueous solution using Mn-WO_3/LED photocatalytic process: Kinetic, mechanism, degradation pathway and toxicity reduction. *Chem. Eng. J.*, 380, 122497. https://doi.org/10.1016/j.cej.2019.122497.

Chen, M., Guo, C., Hou, S., Wu, L., Lv, J., Hu, C., Zhang, Y., Xu, J., 2019. In-situ fabrication of Ag/P-g-C_3N_4 composites with enhanced photocatalytic activity for sulfamethoxazole degradation. *J. Hazard. Mater*, 366, 219-228. https://doi.org/10.1016/j.jhazmat.2018.11.104.

Dong, H., Guo, X., Yang, C., Ouyang, Z., 2018. Synthesis of g-C_3N_4 by different precursors under burning explosion effect and its photocatalytic degradation for tylosin. *Appl. Catal. B Environ*. 230, 65-76. https://doi.org/10.1016/j.apcatb.2018.02.044.

Oh, W. D., Dong, Z., Ronn, G., Lim, T. T., 2017. Surface–active bismuth ferrite as superior peroxymonosulfate activator for aqueous sulfamethoxazole removal: performance, mechanism, and quantification of sulfate radical, *J. Hazard. Mater*, 325, 71-81. https://doi.org/10.1016/j.jhazmat.2016.11.056.

Liu, G., Wang, H., Chen, D., Dai, C., Zhang, Z., Feng, Y., 2020. Photodegradation performances and transformation mechanism of sulfamethoxazole with CeO_2/CN heterojunction as photocatalyst. *Sep. Purif. Technol*., 237, 116329. https://doi.org/10.1016/j.seppur.2019.116329.

Giannakis, S., Samoili, S., Rodriquez-Chueca, J., 2021a. A meta-analysis of the scientific literature on (photo) Fenton and persulfate Advanced Oxidation Processes: where do we stand and where are we heading to? *Curr. Opin. Green Sustain.* 100456. https://doi.org/10.1016/j.cogsc.2021.100456.

Ghanbari, F., Moradi, M., 2017. Application of peroxymonosulfate and its acivation methods for environmental organic pollutants. *Chem. Eng. J.*, 310, 41-62. https://doi.org/10.1016/j.cej.2016.10.064.

Rodriguez-Chueca, J., Giannakis, S., Marjanovic, M., Kohantorabi, M., Gholami, M. R., Grandjean, D., de Alencastro, L. F., Pulgarin, C., 2019. Solar-assisted bacteria disinfection and removal of contaminants of emerging concern by Fe^{2+}-activated HSO_5^- *vs.* $S_2O_8^{2-}$ in drinking water. *Appl. Catal. B: Environ*, 248, 62-72. https://doi.org/10.1016/j.apcatb.2019.02.018.

Li, Y., Li, J., Pan, Y., Xiong, Z., Yao, G., Xie, R., Lai, B., 2020. Peroxymonosulfate activation on $FeCo_2S_4$ modified g-C_3N_4 ($FeCo_2S_4$-CN): Mechanism of singlet oxygen evolution for nonradical efficient degradation of sulfamethoxazole. *Chem. Eng. J.*, 384, 123361. https://doi.org/10.1016/j.cej.2019.123361.

Guo, R., Nengzi, L., Chen, Y., Li, Y., Zhang, X., Cheng, X., 2020a. Efficient degradation of sulfamethoxazole by CuCo LDH and LDH@fibers composite membrane activating peroxymonosulfate. *Chem. Eng. J.*, 398, 125676. https://doi.org/10.1016/j.cej.2020.125676.

Kohantorabi, M., Moussavi, G., Giannakis, S., 2021a. A review of the innovations in metal- and carbon-based catalysts explored for heterogeneous peroxymonosulfate (PMS) activation, with focus on radical vs. non-radical degradation pathways of organic contaminants. *Chem. Eng. J.*, 127957. https://doi.org/10.1016/j.cej.2020.127957.

Xu, N., Zhou, H., Wu, Z., Li, N., Xiong, Z., Yao, G., Lai, B., 2020. Efficient degradation of sulfamethoxazole by $NiCo_2O_4$ modified expanded graphite activated peroxymonosulfate: Characterization, mechanism, and degradation intermediates. *J. Hazard. Mater*, 399, 123103. https://doi.org/10.1016/j.jhazmat.2020.123103.

Giannakis, S., Lin, K. Y. A., Ghanbari, F., 2021b. A review of the recent advances on the treatment of industrial wastewaters by Sulfate Radical-based Advanced Oxidation Processes (SR-AOPs). *Chem. Eng. J.*, 406, 127083. https://doi.org/10.1016/j.cej.2020.127083.

Qi, Y., Qu, R., Liu, J., Chen, J., Al-basher, G., Alsultan, N., Wang, Z., Huo, Z., 2019. Oxidation of flumequine in aqueous solution by UV-ctivated peroxymonosulfate: Kinetics, water matrix effects, degradation products and reaction pathways. *Chemosphere*, 237, 124484. https://doi.org/10.1016/j.chemosphere.2019.124484.

Mirzaei, A., Yerushalmi, L., Chen, Z., Haghighat, F., 2018. Photocatalytic degradation of sulfamethoxazole by hierarchical magnetic ZnO@g-C_3N_4: RSM optimization, kinetic study, reaction pathway and toxicity evaluation. *J. Hazard. Mater*, 359, 516-526. https://doi.org/10.1016/j.jhazmat.2018.07.077.

Zarezadeh, S., Habibi-Yangjeh, A., Mousavi, M., 2019. Fabrication of novel ZnO/BiOBr/C-Dots nanocomposites with considerable photocatalytic performances in removal of organic pollutants under visible light. *Adv. Powder. Technol.*, 30, 1197-1209. https://doi.org/10.1016/j.apt.2019.03.016.

Vosoughi, F., Habibi-Yangjeh, A., Asadzadeh-Khaneghah, S., Ghosh, S., 2020. Novel ternary g-C_3N_4 nanosheet/Ag_2MoO_4/AgI photocatalysts: Impressive photocatalysts for removal of various contaminants. *J. Photochem. Photobiol. A: Chem.*, 403, 112871. https://doi.org/10.1016/j.jphotochem.2020.112871.

Hu, Y., Li, Z., Yang, J., Zhu, H., 2019. Degradation of methylparaben using BiOI-hydrogel composites activated peroxymonosulfate under visible light irradiation. *Chem. Eng. J.*, 360, 200-211. https://doi.org/10.1016/j.cej.2018.11.217.

Zhang, J., Zhao, W., Li, Z., Lu, G., Zhu, M., 2021. Visible-light-assisted peroxymonosulfate activation over Fe(II)/V(IV) self-doped $FeVO_4$ nanobelts with enhanced sulfamethoxazole degradation: Performance and mechanism. *Chem. Eng. J.*, 403, 126384. https://doi.org/10.1016/j.cej.2020.126384.

Shao, H., Zhao, X., Wang, Y., Mao, R., Wang, Y., Qiao, M., Zhao, S., Zhu, Y., 2017. Synergetic activation of peroxymonosulfate by Co_3O_4 modified g-C_3N_4 for enhanced degradation of diclofenac sodium under visible light irradiation. *Appl. Catal. B: Environ*, 218, 810-818. https://doi.org/10.1016/j.apcatb.2017.07.016.

Wetchakun, N., Chaiwichain, S., Inceesungvorn, B., Pingmuang, K., Phanichphant, S., Minett, A. I., 2012. J. Chen. $BiVO_4$/CeO_2 nanocomposites with high visible-light-induced photocatalytic activity. *ACS Appl. Mater. Interfaces*, 4 (7), 3718-3723. https://doi.org/10.1021/am300812n.

Vaseli-Kermani, E., Habibi-Yangjeh, A., Diarmand-Khalilabad, H., Ghosh, S., 2020. Nitrogen photofixation ability of g-C_3N_4 nanosheets/Bi_2MoO_6 heterojunction photocatalyst under visible-light illumination. *J. Colloid. Inter. Sci.*, 563, 81-91. https://doi.org/10.1016/j.jcis.2019.12.057.

Yuan, X., Shen, D., Zhang, Q., Zou, H., Liu, Z., Peng, F., 2019. Z-scheme Bi_2WO_6/$CuBi_2O_4$ heterojunction mediated by interfacial electric field for efficient visible-light photocatalytic degradation of tetracycline. *Chem. Eng. J.*, 369, 292-301. https://doi.org/10.1016/j.cej.2019.03.082.

Gao, X., Tang, G., Peng, W., Guo, Q., Luo, Y., 2019. Surprise in the phosphate modification of BiOCl with oxygen vacancy: In situ construction of hierarchical Z-scheme BiOCl-OV-$BiPO_4$ photocatalyst for the degradation of carbamazepine. *Chem. Eng. J.*, 360, 1320-1329. https://doi.org/10.1016/j.cej.2018.10.216.

Bardos, E., Kiraly, A. K., Pap, Z., Baia, L., Garg, S., Hernadi, K., 2019. The effect of the synthesis temperature and duration on the morphology and photocatalytic activity of BiOX (X=Cl, Br, I) materials. *Appl. Surf. Sci.*, 479, 745-756. https://doi.org/10.1016/j.apsusc.2019.02.136.

Mehraj, O., Pirzad, B. M., Mir, N. A., Khan, M. Z., Sabir, S., 2016. A highly efficient visible-light-driven novel p-n junction Fe_2O_3/BiOI photocatalyst: Surface decoration of BiOI nanosheets with Fe_2O_3 nanoparticles. *Appl. Surf. Sci.*, 387, 642-651. https://doi.org/10.1016/j.apsusc.2016.06.166.

Mousavi, M., Habibi-Yangjeh, A., 2016. Magnetically separable ternary g-C_3N_4/Fe_3O_4/BiOI nanocomposites: Novel visible-light-driven photocatalysts based on graphitic carbon nitride. *J. Colloid. Inter. Sci.*, 465, 83-92. https://doi.org/10.1016/j.jcis.2015.11.057.

Jiang, X., Lai, S., Xu, W., Fang, J., Chen, X., Beiyuan, J., Zhou, X., Lin, K., Liu, J., Guan, G., 2019. Novel ternary BiOI/g-C_3N_4/CeO_2 catalysts for enhanced photocatalytic degradation of tetracycline under visible-light radiation via double charge transfer process. *J. Alloys. Compd.* 809, 151804. https://doi.org/10.1016/j.jallcom.2019.151804.

Raso, R. A., Stepuk, A., Mohn, D., Pounescu, D., Koehler, F. M., Stark, W. J., 2014. Regenerable cerium oxide based odor adsorber for indoor air purification from acidic volatile organic compounds. *Appl. Catal. B: Environ*. 147, 965-972. https://doi.org/10.1016/j.apcatb.2013.10.030.

Wen, X. J., Niu, C. G., Huang, D. W., Zhang, L., Liang, C., Zeng, G. M., 2017. Study of the photocatalytic degradation pathway of norfloxacin and mineralization activity using a novel ternary Ag/AgCl-CeO_2 photocatalyst. *J. Catal*. 355, 73-86. https://doi.org/10.1016/j.jcat.2017.08.028.

Wang, H., Liao, B., Lu, T., Ai, Y., Liu, G., 2020a. Enhanced visible-light photocatalytic degradation of tetracycline by a novel hollow BiOCl@CeO_2 heterostructured microspheres: Structural characterization and reaction mechanism. *J. Hazard. Mater*, 385, 121552. https://doi.org/10.1016/j.jhazmat.2019.121552.

Khavar, A. H. C., Moussavi, G., Mahjoub, A., Yaghmaeian, K., Srivastava, V., Sillanpaa, M., Satari, M., 2019. Novel magnetic Fe_3O_4@rGO@ZnO onion-like microspheres decorated with Ag nanoparticles for the efficient photocatalytic oxidation of metformin: toxicity evaluation and insights into the mechanisms. *Catal. Sci. Technol*., 9, 5819. https://doi.org/10.1039/C9CY01381D.

Kohantorabi, M., Gholami, M. R., 2018a. Cyclohexene oxidation catalyzed by flower-like core-shell Fe_3O_4@Au/metal organic frameworks nanocomposite. *Mater. Chem. Phys*., 213, 472-481. https://doi.org/10.1016/j.matchemphys.2018.04.051.

Ghanbari, F., Ahmadi, M., Gohari, F., 2019. Heterogeneous activation of peroxymonosulfate via nanocomposite CeO_2-Fe_3O_4 for organic pollutants removal: The effect of UV and US irradiation and application for real wastewater. *Sep. Purif. Technol*., 228, 115732. https://doi.org/10.1016/j.seppur.2019.115732.

Boruah, P. K., Sharma, B., Karbhal, I., Shelke, M. V., Das, M. R., 2017. Ammonia-modified graphene sheets decorated with magnetic Fe_3O_4 nanoarticles for the photocatalytic and photo-Fenton degradation of phenolic compounds under sunlight irradiation. *J. Hazard. Mater*, 325, 90-100. https://doi.org/10.1016/j.jhazmat.2016.11.023.

Vogel, A. I., Vogel's Textbook of Quantitative Chemical, Longman Scientic &Technical, London, 1989.

Kohantorabi, M., Gholami, M. R., 2018b. Fabrication of novel ternary Au/CeO_2@g-C_3N_4 nanocomposite: kinetics and mechanism investigation of 4-nitrophenol reduction, and benzyl alcohol oxidation. *Appl. Phys. A.*, 441, 124. https://doi.org/10.1007/s00339-018-1858-0.

Reza, N., Reza, W., Gul, H., Azam, M., Lee, J., Vikrant, K., Kim, K. H., 2020. Solar-light-active silver phosphate/titanium dioxide/silicaheterostructures for photocatalytic removal of organic dye. *J. Clean. Product*, 254, 120031. https://doi.org/10.1016/j.jclepro.2020.120031.

Vikrant, K., Park, C. M., Kim, K. H., Kumar, S., Jeon, E. C., 2019. Recent advancement in photocatalyst-based platforms for the destruction of gaseous benzene: Performance evaluation of different modes of photocatalytic operations and against adsorption technique. *J. Photochem. Photobio C.* 41, 100316. https://doi.org/10.1016/j.jphotochemrev.2019.08.003.

Zhong, S., Wang, B., Zhou, H., Li, C., Peng, X., Zhang, S., 2019. Fabrication and characterization of Ag/BiOI/GO composites with enhanced photocatalytic activity. *J. Alloy. Compound*, 806, 401-409. https://doi.org/10.1016/j.jallcom.2019.07.223.

Wang, K., Chang, Y. Q., Lv, L., Long, Y., 2015. Effect of annealing temperature on oxygen vacancy concentrations of nanocrystalline CeO_2 film. *Appl. Surf. Sci*., 351, 164-168. https://doi.org/10.1016/j.apsusc.2015.05.122.

Hou, J., Jiang, K., Shen, M., Wei, R., Wu, X., Idrees, F., Cao, C., 2017. Micro and nano hierarchical structures of BiOI/activated carbon for efficient visible-light-photocatalytic reactions. *Sci Rep*., 7 (1), 11665. https://doi.org/10.1038/s41598-017-12266-x.

Salari, H., Kohantorabi, M., 2020. Fabrication of novel Fe_2O_3/MoO_3/AgBr nanocomposites with enhanced photocatalytic activity under visible light irradiation for organic pollutant degradation. *Adv. Powder. Technol*., 31 (1), 493-503. https://doi.org/10.1016/j.apt.2019.11.005.

Huang, Z., Wu, P., Gong, B., Zhang, X., Liao, Z., Chiang, p. C., Hu, X., Cu, L., 2017. Immobilization of visible light-sensitive (N, Cu) co-doped TiO_2 onto rectorite for photocatalytic degradation of p-chlorophenol in aqueous solution. *Appl. Clay Sci*. 142, 128-135. https://doi.org/10.1016/j.clay.2016.10.010.

Kohantorabi, M., Giannakis, S., Moussavi, G., Bensimon, M., Gholami, M. R., Pulgarin, C., 2021b. An innovative, highly stable Ag/ZIF-67@GO nanocomposite with exceptional peroxymonosulfate (PMS) activation efficacy, for the destruction of chemical and microbiological contaminants under visible light, *J. Hazard. Mater*, 413, 125308. https://doi.org/10.1016/j.jhazmat.2021.125308.

Ozores Diez, P., Giannakis, S., Rodriguez-Chueca, J., Wang, D., Quilty, B., Devery, R., McGuigan, K., Pulgarin, C., 2020. Enhancing solar disinfection (SODIS) with the photo-Fenton or the Fe^{2+}/peroxymonosulfate-activation process in large-scale plastic bottles leads to toxicologically safe drinking water. *Water. Res.*, 186, 116387. https://doi.org/10.1016/j.watres.2020.116387.

Xu, L., Wang, J., 2012. Magnetic nanoscaled Fe_3O_4/CeO_2 composite as an efficient Fenton like heterogeneous catalyst for degradation of 4-chlorophenol, *Environ. Sci. Technol*. 46, 10145-10153. https://doi.org/10.1021/es300303f.

He, Y., Zhang, J., Zhou, H., Yao, G., Lai, B., 2020. Synergistic multiple active species for the degradation of sulfamethoxazole by peroxymonosulfate in the presence of CuO@FeO_x@Fe^0. *Chem. Eng. J.*, 380, 122568. https://doi.org/10.1016/j.cej.2019.122568.

Wang, S., Liu, Y., Wang, J., 2020b. Iron and sulfur co-doped graphite carbon nitride (FeO_y/S-g-C_3N_4) for activating peroxymonosulfate to enhance sulfamethoxazole degradation. *Chem. Eng. J.*, 382, 122836. https://doi.org/10.1016/j.cej.2019.122836.

Guo, R., Wang, Y., Li, J., Cheng, X., Dionysiou, D. D., 2020b. Sulfamethoxazole degradation by visible light assisted peroxymonosulfate process based on nanohybrid manganese dioxide incorporating ferric oxide. *Appl. Catal. B: Environ*, 278, 119297. https://doi.org/10.1016/j.apcatb.2020.119297.

Zhang, J., Zhai, C., Zhao, W., Chen, Y., Yin, R., Zeng, L., Zhu, M., 2020. Insight into combining visible-light photocatalysis with transformation of dual metal ions for enhancing peroxymonosulfate activation over dibismuth copper oxide. *Chem. Eng. J.*, 397, 125310. https://doi.org/10.1016/j.cej.2020.125310.

Wang, S., Xu, W., Wu, J., Gong, Q., Xie, P., 2020c. Improved sulfamethoxazole degradation by the addition of MoS_2 into the Fe^{2+}/peroxymonosulfate process. *Sep. Purif. Technol.*, 235, 116170. https://doi.org/10.1016/j.seppur.2019.116170.

Lu, H., Sui, M., Yuan, B., Wang, J., Lv, Y., 2019. Efficient degradation of nitrobenzene by Cu-Co-Fe-LDH catalyzed peroxymonosulfate to produce hydroxyl radicals. *Chem. Eng. J.*, 357, 140-149. https://doi.org/10.1016/j.cej.2018.09.111.

Yang, L., Liang, L., Wang, L., Zhu, J., Gao, S., Xia, X., 2019. Accelerated photocatalytic oxidation of carbamazepine by a novel 3D hierarchical protonated g-C_3N_4/BiOBr heterojunction: Performance and mechanism. *Appl. Surf. Sci.* 473, 527-539. https://doi.org/10.1016/j.apsusc.2018.12.180.

Hong, Y., Zhou, H., Xiong, Z., Liu, Y., Yao, G., Lai, B., 2020. Heterogeneous activation of peroxymonosulfate by CoMgFe-LDO for degradation of carbamazepine: Efficiency, mechanism, and degradation pathways. *Chem. Eng. J.*, 391, 123604. https://doi.org/10.1016/j.cej.2019.123604.

Zhai, Y., Zheng, F., Zhao, X., Xia, X., Teng, Y., 2019. Identification of hydrochemical genesis and screening of typical groundwater pollutants impacting human health: A case study in Northeast China. *Environ. Pollut*. 252, 1202-1215. https://doi.org/10.1016/j.envpol.2019.05.158.

Guo, F., Chen, J., Zhao, J., Xia, D., Zhan, Z., Wang, Q., 2020c. Z-scheme heterojunction g-C_3N_4@PDA/BiOBr with biomimetic polydopamine as electron transfer mediators for enhanced visible-light driven degradation of sulfamethoxazole. *Chem. Eng. J.*, 386, 124014. https://doi.org/10.1016/j.cej.2020.124014.

Wang, J., Guo, H., Liu, Y., Li, W., Yang, B., 2020d. Peroxymonosulfate activation by porous $BiFeO_3$ for the degradation of bisphenol AF: Non-radical and radical mechanism. *Appl. Surf. Sci.*, 507, 145097. https://doi.org/10.1016/j.apsusc.2019.145097.

Moradi, M., Moussavi, G., Yaghmaeian, K., Yazdanbakhsh, A., Srivastava, V., Sillanpaa, M., 2020. Synthesis of novel Ag-doped S-MgO nanosphere as an efficient UVA/LED activated photocatalyst for non-radical oxidation of diclofenac: Catalyst preparation and characterization and photocatalytic mechanistic evaluation. *Appl. Catal. B: Environ*. 260, 118128. https://doi.org/10.1016/j.apcatb.2019.118128.

Rommozzi, E., Giannakis, S., Giovannetti, R., Vione, D., Pulgarin, C., 2020. Detrimental vs. beneficial influence of ions during solar (SODIS) and photo-Fenton disinfection of E. coli in water: (Bi)carbonate, chloride, nitrate, and nitrite effects. *Appl. Catal. B: Environ*. 270, 118877. https://doi.org/10.1016/j.apcatb.2020.118877.

Li, J., Fang, J., Ye, P., Wu, D., Wang, M., Li, X., Xu, A., 2017. Peroxymonosulfate activation by iron oxide modified g-C_3N_4 under visible light for pollutants degradation. *J. Photochem. Photobiol. Chem.*, 342, 85-93. https://doi.org/10.1016/j.jphotochem.2017.04.004.

Liu, Y., Xu, J., Wang, L., Zhang, H., Xu, P., Duan, X., Sun, H., Wang, S., 2017. Three-Dimensional BiOI/BiOX (X=Cl or Br) nanohybrids for enhanced visible-light photocatalytic activity. *Nanomaterials*, 7(3), 64. https://doi.org/10.3390/nano7030064.

Kohantorabi, M., Hosseinifard, M., Kazemzadeh, A., 2020. Catalytic activity of magnetic Fe_2O_3@$CoFe_2O_4$ nanocomposite in peroxymonosulfate activation for norfloxacin removal. *New J. Chem.*, 44, 4185-4198. https://doi.org/10.1039/C9NJ04379A.

Yang, Y., Lu, X., Jiang, J., Ma, J., Liu, G., Cao, Y., Liu, W., Li, J., Pang, S., Kong, X., Luo, C., 2017. Degradation of sulfamethoxazole by UV, UV/H_2O_2 and UV/persulfate (PDS): Formation of oxidation products and effect of bicarbonate, *Water Res*. 118, 196-207. https://doi.org/10.1016/j.watres.2017.03.054.